SUBMITTED TO APJ 1 AUG 2007, ACCEPTED 23 OCT 2007.
Preprint typeset using LaTeX style emulateapj v. 03/07/07

arXiv:0710.4294v3 [astro-ph] 21 Dec 2007

LONG-TERM COLLISIONAL EVOLUTION OF DEBRIS DISKS

TORSTEN LÖHNE AND ALEXANDER V. KRIVOV
Astrophysikalisches Institut und Universitätssternwarte, Friedrich Schiller University Jena, Schillergäßchen 2–3, 07745 Jena, Germany;
tloehne@astro.uni-jena.de, krivov@astro.uni-jena.de

JENS RODMANN
SCI-SA, Research and Scientific Support Department of ESA, ESTEC, 2200 AG Noordwijk, The Netherlands; jrodmann@rssd.esa.int
Submitted to ApJ 1 Aug 2007, accepted 23 Oct 2007.

ABSTRACT

Infrared surveys indicate that the dust content in debris disks gradually declines with stellar age. We simulated the long-term collisional depletion of debris disks around solar-type (G2 V) stars with our collisional code. The numerical results were supplemented by, and interpreted through, a new analytic model. General scaling rules for the disk evolution are suggested. The timescale of the collisional evolution is inversely proportional to the initial disk mass and scales with radial distance as $r^{4.3}$ and with eccentricities of planetesimals as $e^{-2.3}$. Further, we show that at actual ages of debris disks between 10 Myr and 10 Gyr, the decay laws of the dust mass and the total disk mass are different. The reason is that the collisional lifetime of planetesimals is size-dependent. At any moment, there exists a transitional size, which separates larger objects that still retain the "primordial" size distribution set in the growth phase from smaller objects whose size distribution is already set by disruptive collisions. The dust mass and its decay rate evolve as that transition affects objects of ever-larger sizes. Under standard assumptions, the dust mass, fractional luminosity, and thermal fluxes all decrease as t^{ξ} with $\xi = -0.3...-0.4$. Specific decay laws of the total disk mass and the dust mass, including the value of ξ, largely depend on a few model parameters, such as the critical fragmentation energy as a function of size, the primordial size distribution of largest planetesimals, as well as the characteristic eccentricity and inclination of their orbits. With standard material prescriptions and a distribution of disk masses and extents, a synthetic population of disks generated with our analytic model agrees quite well with the observed Spitzer/MIPS statistics of 24 and 70 μm fluxes and colors versus age.

Subject headings: circumstellar matter — planetary systems: formation.

1. INTRODUCTION

Since the IRAS discovery of the excess infrared emission around Vega by Aumann et al. (1984), subsequent infrared surveys with ISO, Spitzer and other instruments have shown the Vega phenomenon to be common for main-sequence stars. The observed excess is attributed to second-generation circumstellar dust, produced in a collisional cascade from planetesimals and comets down to smallest grains that are blown away by the stellar radiation. While the bulk of such a debris disk's mass is hidden in invisible parent bodies, the observed luminosity is dominated by small particles at dust sizes. Hence the studies of dust emission offer a natural tool to gain insight into the properties of planetesimal populations as well as planets that may shape them and, ultimately, into the evolutionary history of circumstellar planetary systems.

In recent years, various photometric surveys of hundreds of nearby stars have been conducted with the Spitzer Space Telescope. These are the GTO survey of FGK stars (Beichman et al. 2005; Bryden et al. 2006; Beichman et al. 2006a), the FEPS Legacy project (Meyer et al. 2004; Kim et al. 2005), the A star GTO programs (Rieke et al. 2005; Su et al. 2006), the young cluster programs (Gorlova et al. 2006), and others. These observations were done mostly at 24 and 70 μm with the MIPS photometer, but also between 5 and 40 μm with the IRS spectrometer (Jura et al. 2004; Chen et al. 2006). Based on these studies, about 15% of mature solar-type (F0–K0) stars have been found to harbor cold debris disks at 70 μm. For cooler stars, the fraction drops to 0%–4% (Beichman et al. 2006a). For earlier spectral types, the proportion increases to about 33% (Su et al. 2006). At 24 μm, the fraction of systems with detected excess stays similar for A stars, but appreciably decreases for FGK ones. Similar results in the sub-millimeter range are expected to become available soon from a survey with SCUBA and SCUBA2 on JCMT (Matthews et al. 2007). Preliminary SCUBA results for M dwarfs suggest, in particular, that the proportion of debris disks might actually be higher than suggested by Spitzer (Lestrade et al. 2006).

All authors point out a decay of the observed infrared excesses with systems' age. However, the values reported for the slope of the decay, assuming a power-law dependence $t^{-\alpha}$, span a wide range. Greaves & Wyatt (2003) suggest $\alpha \lesssim 0.5$, Liu et al. (2004) give $0.5 < \alpha < 1.0$, Spangler et al. (2001) report $\alpha \approx 1.8$, and Greaves (2005) and Moór et al. (2006) derive $\alpha \approx 1.0$. Fits of the upper envelope of the distribution of luminosities over the age yield $\alpha \approx 1.0$ as well (Rieke et al. 2005). Besides, the dust fractional luminosity exhibits a large dispersion at any given age.

In an attempt to gain theoretical understanding of the observed evolution, Dominik & Decin (2003) assumed that equally-sized "comets" produce dust through a cascade of subsequent collisions among ever-smaller objects. If this dust is removed by the same mechanism, the steady-state amount of dust in such a system is proportional to the number of comets. This results in an $M/M_0 \approx \tau/t$ dependence for the amount of dust and for the number of comets or the total mass of the disk. Under the assumption of a steady state, this result is valid even for more complex systems with continuous size distributions from planetesimals to dust. Tenuous disks, where the lifetime of dust grains is not limited by collisions

but by transport processes like the Poynting-Robertson drag (Artymowicz 1997; Krivov et al. 2000; Wyatt 2005), follow $M \propto t^{-2}$ rather than $M \propto t^{-1}$.

More recently, Wyatt et al. (2007a) lifted the most severe simplifying assumption of the Dominik-Decin model, that of equal-sized parent bodies, and included them into the collisional cascade. A debris disk they consider is no longer a two-component system "comets + dust". Instead, it is a population of solids with a continuous size distribution, from planetesimals down to dust. A key parameter of the description by Dominik & Decin (2003) is the collisional lifetime of comets, τ. Wyatt et al. (2007a) replaced it with the lifetime of the largest planetesimals and worked out the dependencies on this parameter in great detail. Since the collisional timescale is inversely proportional to the amount of material, $\tau \propto 1/M_0$, the asymptotic disk mass becomes independent of its initial mass. Only dynamical quantities, i.e. the disk's radial position and extent, the orbiting objects' eccentricities and inclinations, and material properties, i.e. the critical specific energy and the disruption threshold, as well as the type of the central star determine the very-long-term evolution.

Still, there are two important simplifications made in the model by Wyatt et al. (2007a): (i) the disk is assumed to be in collisional equilibrium at all sizes, from dust up to the largest planetesimals and (ii) the minimum specific energy needed to disrupt colliding objects is independent of their size. As a consequence of (i) and (ii), the size distribution of solids is a single power-law. To check how reasonable these assumptions are, realistic simulations of the disks with collisional codes are necessary (e.g., Thébault et al. 2003; Krivov et al. 2005, 2006; Thébault & Augereau 2007).

The aim of this paper is two-fold. First, we follow the evolution of debris disks with our elaborate numerical code (Krivov et al. 2005, 2006) to check the existing analytic models and the assumptions (i) and (ii) they are based upon. Second, in order to make these numerical results easier to use, we develop a new analytic model for the evolution of disk mass and dust mass that relaxes both assumptions (i) and (ii) above.

Section 2 summarizes the basic ideas and assumptions and describes our numerical model and the runs of the collisional code. In Section 3 the numerical results are presented and dependences of the collisional timescale on the disk mass, distance to the star, and mean eccentricity of parent bodies are derived. In section 4, the analytic model for the evolution of disk mass and dust mass is developed. Section 5 analyzes the evolution of dust luminosities. In Section 6, we use the analytic model to synthesize representative populations of debris disks and compare them with statistics of debris disks derived from the Spitzer surveys. A summary is given and conclusions are drawn in Section 7.

2. NUMERICAL MODEL AND DESCRIPTION OF RUNS

2.1. *Basic Approach*

For all numerical runs in this paper, we use a C++-based collisional code (ACE, Analysis of Collisional Evolution). The code numerically solves the Boltzmann-Smoluchowski kinetic equation to evolve a disk of solids in a broad range of sizes (from sub-micrometers to about a hundred of kilometers), orbiting a primary in nearly-Keplerian orbits (gravity + direct radiation pressure + drag forces) and experiencing disruptive collisions. Collisions are simulated with available material- and size-dependent scaling laws for fragmentation and dispersal in both strength and gravity regime. The current version implements a 3-dimensional kinetic model, with masses, semi-major axes, and eccentricities as phase space variables. This approach automatically enables a study of the simultaneous evolution of mass, spatial, and velocity distribution of particles. The code is fast enough to easily follow the evolution of a debris disk over Gyr timescales. A detailed description of our approach, its numerical implementation, and astrophysical applications can be found in our previous papers (Krivov et al. 2000, 2005, 2006).

2.2. *Disruption Threshold and Critical Specific Energy*

An object is said to be disrupted in a collision, if the largest fragment is at most half as massive as the original object. If the impactor's relative velocity is so high that the ratio of impact energy and target mass exceeds the target's critical specific energy, $Q^*_{\rm D}$, the target (and the impactor) are disrupted. For small objects, this binding energy is dominated by material strength, and for larger objects, self-gravity takes over. Both regimes are usually described by a sum of two power laws (Krivov et al. 2005, Sect. 5.1, and references therein)

$$Q^*_{\rm D} = A_{\rm s} \left(\frac{s}{1\,{\rm m}}\right)^{3b_{\rm s}} + A_{\rm g} \left(\frac{s}{1\,{\rm km}}\right)^{3b_{\rm g}}, \qquad (1)$$

where "s" and "g" stand for strength and gravity, respectively. The reported values of the coefficients $A_{\rm s}$ and $A_{\rm g}$ vary by more than one order of magnitude, and we took $A_{\rm s} = A_{\rm g} = 5 \times 10^6$ erg/g, in agreement with the reference case for basalt given by Benz & Asphaug (1999). The exponents are $3b_{\rm s} = -0.3$ and $3b_{\rm g} = 1.5$ (corresponding to -0.1 and 0.5 in the mass scaling). With these parameters, the two power-law components contribute equally at $s \approx 316$ m, and the lowest binding energy, the minimum $Q^*_{\rm D}$, is reached at $s \approx 129$ m. The influence of the choice of parameters on the resulting evolution is discussed in Sect. 4.

For computational reasons, we refrained from including a treatment of cratering collisions in the runs. Note that these were not taken into account in previous studies of the long-term evolution of debris disks (e.g. Dominik & Decin 2003; Wyatt et al. 2007a) either. Thébault et al. (2003) and Thébault & Augereau (2007), who focused on shorter time spans, did include this non-disruptive type of collisions that lead to the continuous erosion of a target by small impacting projectiles. They found the effect to be dominant for particles in between 100 μm and 1 cm for the case of the inner β Pictoris disk, while big, kilometer-sized objects in the gravity regime are mainly lost to disruptive collisions (see Table 4 in Thébault et al. 2003). However, including cratering can lower the lifetime of large objects, especially when relative velocities are low and disruptive collisions are rare. Another caveat is that cratering collisions alter the shape of the wavy size distribution at the lower end (Thébault & Augereau 2007), which affects the observable thermal fluxes.

2.3. *Collisional Outcomes*

The distribution of sizes and the velocities of fragments in an individual (catastrophic) collision has been subject to studies for decades. Laboratory work was done on high-velocity impacts on scales of millimeters and centimeters (e.g., Fujiwara et al. 1977; Fujiwara 1986; Davis & Ryan 1990). Statistics on the mass distributions of observed asteroidal families and geometrical considerations (Paolicchi et al. 1996; Tanga et al. 1999; Tedesco et al. 2005) as well as gravito-hydrodynamic simulations of fragmentation and reaccumulation (Michel et al. 2002) cover the range of larger, kilometer-sized bodies. On small scales, the resulting size distributions show a strong dependence on impact velocity and seem to indicate a turn in the power law at fragment sizes around $\approx$ 1 mm (or $\approx$ 1% of the size of the used targets). The slope for objects above that size is steeper than the one for smaller objects (Davis & Ryan 1990). However, Thébault et al. (2003) found that the ratio of these two slopes and the size at which the slope changes influence simulation results only slightly. On kilometer and larger scales, the fragmentation is influenced by gravitational reaccumulation of relatively small fragments onto bigger ones. Hence, bigger fragments ($\sim$ 100km) will be overabundant, and conversely, smaller fragments ($\sim$ 1km) underabundant, compared to the underlying distribution without gravity. The slopes of the size distribution $n(s) \propto s^{-p}$ of kilometer-sized objects are poorly known. A wide range from $p = 3.5$ up to $p = 9.0$ has been reported. These deviations in the kilometer regime are most probably the severest caveat of the power-law approximation, because they are independent of the actual material and caused only by gravity. Nevertheless, we assume that fragments follow a single power-law distribution $n_{\rm frag}(s) \propto s^{-3.5}$, expecting the influence on the final collisional steady state to be only moderate.

2.4. *Commons for All Runs*

All disk models presented here are set up around a star of solar mass and luminosity. Parameters of the central star affect the disk evolution in various ways. They determine the size limit for grain's blowout by radiation pressure and orbital velocities at a given distance, thereby altering impact velocities and rates. For late-type stars, strong stellar winds may affect the dust dynamics (Augereau & Beust 2006; Strubbe & Chiang 2006). On the observational side, dust temperatures and brightnesses are influenced. Here, we focus on the scalings for a fixed spectral type (G2V), and not on scalings between different types.

The disks themselves all share the same material properties and shapes. We adopt the material, described by a bulk density $\rho = 2.5$ g/cm^3, the radiation pressure efficiency of astronomical silicate (Laor & Draine 1993), and a critical fragmentation energy as specified in Sect. 2.2. We switched off the Poynting-Robertson effect, which is unimportant for debris disks under study, as well as stellar wind drag, which plays only a minor role around G-type stars. The fragments produced in an individual collision are distributed according to a single power law, $\mathrm{d}N \propto s^{-3.5}\mathrm{d}s \propto m^{-11/6}\mathrm{d}m$. A biggest fragment size is assumed to scale with specific impact energy to the power of 1.24 (for details, see Krivov et al. 2006). The initial mass distribution is given by $\mathrm{d}N \propto m^{-q}$, with $q = 1.87$, a value that accounts for the modification of the classical Dohnanyi's (1969) $q = 1.833$ through the size dependence of material strength (see, e.g., Durda & Dermott 1997). The particle masses range from 4.2×10^{-15} g, corresponding to a radius of 74 nm, to 4.2×10^{21} g, corresponding to 74 km. The stepping between the 60 mass bins is logarithmic with a factor of ≈ 4 between neighboring bins. The initial radial profile of the particle density was given by a slope of the normal optical depth of -1.0. The initial total mass of each disk was set to 1 $M_\oplus$ (earth mass).

TABLE 1
DESCRIPTION OF NUMERICAL RUNS.

Run	Distance [AU]	$e_{\max}$
Nominal runs		
ii-0.3	7.5–15	0.3
i-0.3	15–30	0.3
o-0.3	30–60	0.3
oo-0.3	60–120	0.3
Additional runs		
i-0.1	15–30	0.1
i-0.2	15–30	0.2
i-0.4	15–30	0.4

2.5. *Specifics of Individual Runs*

We have made four "nominal" runs, each of which corresponds to a certain radial part of the disk between 7.5 and 120 AU from the star (Table 1). In these runs we assumed initial eccentricities of planetesimals to be uniformly distributed between $e_{\min} = 0.0$ and $e_{\max} = 0.3$, spanning three bins centered at 0.05, 0.15 and 0.25. In addition, three runs with altered maximum eccentricity of 0.1, 0.2, and 0.4 were made for the 15–30 AU ring. In all the runs, we assumed that orbital inclinations are distributed between $I_{\min} = e_{\min}/2$ and $I_{\max} = e_{\max}/2$ in accordance with the energy equipartition relation $I = e/2$.

3. NUMERICAL RESULTS AND SCALING LAWS

3.1. *Evolution of Disks of Different Masses*

A debris disk is said to be in a quasi-steady state or quasi-equilibrium if the amounts of particles with different sizes on different orbits, while changing with time (therefore "quasi"), stay constant relative to each other. For brevity, we will often omit "quasi" and use simply "steady state" or "equilibrium". To express the condition of a quasi-steady state formally, we can introduce a phase space, in which a dynamical state of each particle is characterized by a vector $\mathbf{p}$. That vector may be composed, for instance, of coordinates and velocity components. Alternatively, $\mathbf{p}$ may represent the set of orbital elements of the object. Let $n(\mathbf{p}, s, t)$ be the number of objects with radii in $[s, s + \mathrm{d}s]$ at phase space "positions" $[\mathbf{p}, \mathbf{p} + \mathrm{d}\mathbf{p}]$ that the disk contains at the time instant t. The assumption of a quasi-steady state can now be expressed as

$$n(\mathbf{p}, s, t) = \tilde{n}(\mathbf{p}, s)\, f(t). \tag{2}$$

The total disk mass,

$$M_{\rm disk}(t) = \int\int n(\mathbf{p}, s, t)\mathrm{d}\mathbf{p}\mathrm{d}s, \tag{3}$$

can be rewritten as

$$M_{\rm disk}(t) = f(t) \int\int \tilde{n}(\mathbf{p}, s)\mathrm{d}\mathbf{p}\mathrm{d}s \tag{4}$$

or, setting $f(0) = 1$,

$$M_{\rm disk}(t) = f(t) M_0, \tag{5}$$

where M_0 is the initial disk mass. As long as objects are both created and lost in two-particle collisions, their gain and loss rates are given by

$$\dot{n}(\mathbf{p},s,t) = \int\int\int\int [G(\mathbf{p},s,\mathbf{p}_1,s_1,\mathbf{p}_2,s_2) - L(\mathbf{p}_1,s_1,\mathbf{p}_2,s_2)\delta(\mathbf{p}-\mathbf{p}_1)\delta(s-s_1)] \times \tilde{n}(\mathbf{p}_1,s_1)\, f(t)\, \tilde{n}(\mathbf{p}_2,s_2)\, f(t) \times \mathrm{d}\mathbf{p}_1\mathrm{d}s_1\mathrm{d}\mathbf{p}_2\mathrm{d}s_2, \quad (6)$$

where the function $G(\mathbf{p},s,\mathbf{p}_1,s_1,\mathbf{p}_2,s_2)$ describes the gain in population $\mathbf{p}$, s due to collisions between $\mathbf{p}_1$, s_1 and $\mathbf{p}_2$, s_2 and the function $L(\mathbf{p}_1,s_1,\mathbf{p}_2,s_2)$ accounts for the loss in population $\mathbf{p}_1$, s_1 in collisions with $\mathbf{p}_2$, s_2. The disk mass changes at a rate

$$\dot{M}_{\rm disk}(t) = \int\int \dot{n}(\mathbf{p},s,t)\mathrm{d}\mathbf{p}\mathrm{d}s \quad (7)$$

or

$$\dot{M}_{\rm disk}(t) = \dot{f}(t)\int\int \tilde{n}(\mathbf{p},s)\mathrm{d}\mathbf{p}\mathrm{d}s. \quad (8)$$

From Eqs. (6) and (7), we find that $\dot{M}_{\rm disk}(t) \propto f^2(t)$, while Eq. (8) suggests $\dot{M}_{\rm disk}(t) \propto \dot{f}(t)$. Hence, $\dot{f}(t) \propto f^2(t)$. Integration yields

$$f = \frac{1}{1+t/\tau}. \quad (9)$$

Using Eq. (5) we obtain

$$M_{\rm disk}(t) = \frac{M_0}{1+t/\tau} \quad (10)$$

and

$$\dot{M}_{\rm disk}(t) = -CM_{\rm disk}^2, \quad (11)$$

where $1/C = M_0 \cdot \tau$, i.e. the product of the initial mass and a characteristic time. This relation is invariant under the transformation $(t, M_{\rm disk}) \rightarrow (t\cdot x, M_{\rm disk}/x)$, even if C is not constant. Therefore, the mass scale of a system under collisional evolution is inversely proportional to its timescale. For example, doubling the initial total mass halves the collisional lifetime of the system. All curves in the $M_{\rm disk}(t)$ plots can be shifted along lines of equal $t \cdot M_{\rm disk}$.

Dominik & Decin (2003) used this approach and equated the characteristic time τ with the collisional lifetime of their "comets". At the initial phase $t \ll \tau$, Eq. (10) gives

$$M_{\rm disk}(t) \approx M_0\,(1-t/\tau)\,. \quad (12)$$

If the system is old enough so that $t \gg \tau$, the total mass will be just proportional to t^{-1}. Particles whose lifetimes are independent of the total mass are exempt from the asymptotic one-over-t behavior. Examples would be the β-meteoroids that are blown out and small particles in disks tenuous enough for the Poynting-Robertson effect to be more efficient than collisions. The total mass of such particles is $\propto t^{-2}$ (Dominik & Decin 2003).

As we have shown, for the systems that undergo a steady-state collisional evolution, the factor C in Eq. (11) (or τ) should be constant. To check this, we evaluated $C = -\dot{M}_{\rm disk}/M_{\rm disk}^2$ for every two subsequent time steps of the numerical runs. The results are given in Fig. 1.

Instead of being constant at later times, C decreases, roughly following a power law $C \propto t^{-2/3\ldots-4/5}$. The explanation is simple: the systems did not reach an equilibrium where $t \gg \tau$ or at least $t \approx \tau$ during their lifetime. The evolution of the total mass in Fig. 2 demonstrates that as well.

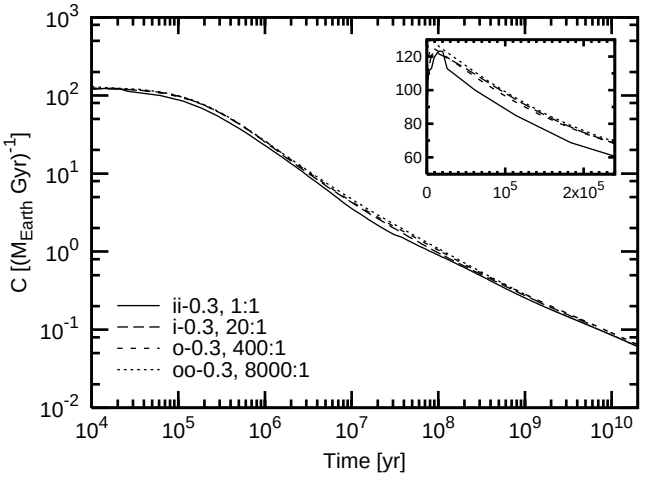


FIG. 1.— The coefficient C from Eq. (11) as a function of time for four nominal runs. The total disk mass and time in the runs are scaled according to $M_{\rm disk} \propto t^{-1}$ to compensate for the difference in dynamical timescale. Note that the near-constancy of C at the beginning of the evolution is an artefact of the double-logarithmic plotting. The double-linear inset shows that the decrease of C is *fastest* at earlier times.

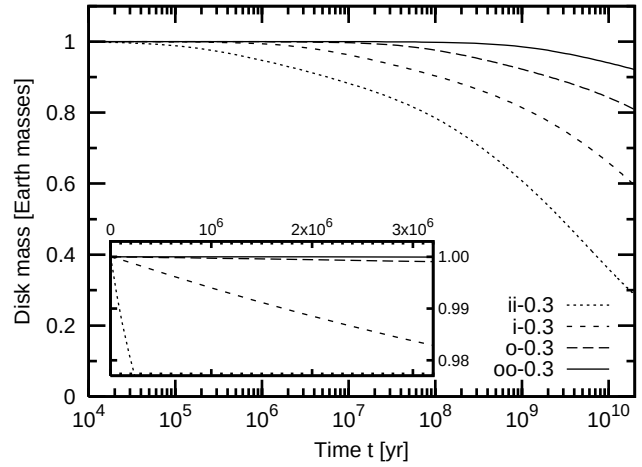


FIG. 2.— The evolution of the total mass in the four nominal runs. Again, the plateau at the beginning of the evolution is an artefact of the logarithmic plotting of time. In fact, the mass decay is strongest at the very beginning (see inset and Eqs. (10), (12)).

3.2. *Dependence on Distance from the Star*

Rings of identical mass but at different distances have different collisional timescales. The comparison in Fig. 1 shows that doubling the distance requires a 20-fold increase in disk mass to have the same timescale. This corresponds to a power-law dependence

$$C \propto r^{-4.3}. \quad (13)$$

In a thorough analytic approach based on a Dohnanyi-type collisional cascade, Wyatt et al. (2007a) came up with $C \propto r^{-13/3}$, which is in good agreement with our numerical result. This index is made up of three contributions. First, the density in the rings drops with r^{-3} as their circumference, height, and width increase linearly. Second, the relative velocities have an $r^{-1/2}$ dependence. Third, these impact velocities affect the minimum required mass for a projectile to be disruptive and thereby the total number of such projectiles. That gives another r^{1-q}, where q is the slope in the appropriate mass

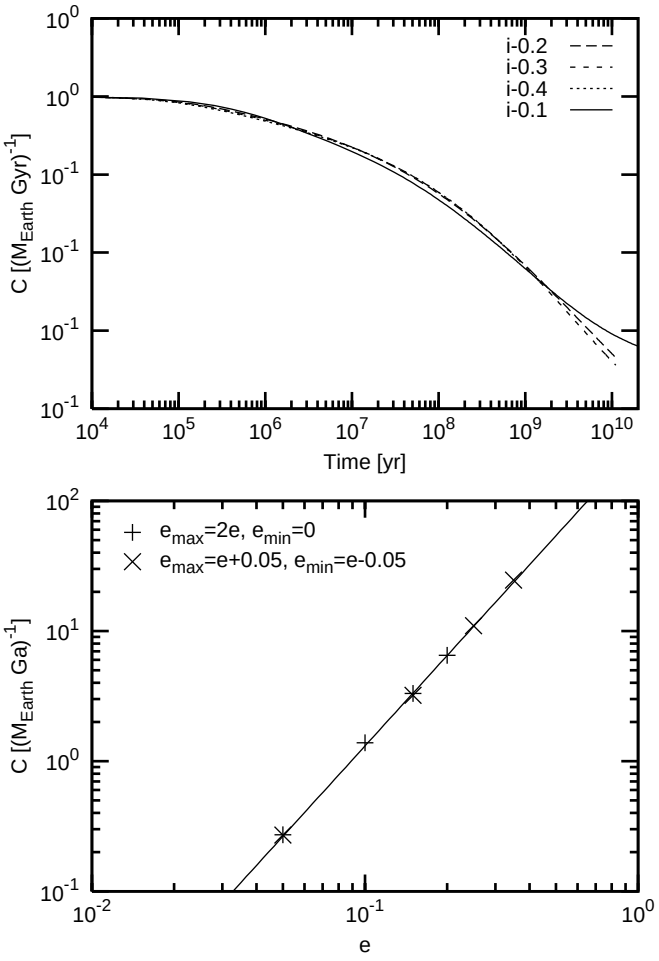


FIG. 3.— The influence of the average eccentricity of planetesimals on the timescale of disk's collisional evolution. *Top:* the evolution of the parameter C from Eq. (11) for four different runs (i-0.1, ..., i-0.4). *Bottom:* four initial C values versus average eccentricity $e = (e_{\max} + e_{\min})/2$ (pluses) together with the $C \propto e^{9/4}$ fit for those runs (line) and the same for runs with a narrower range of eccentricities, as described in Sect. 3.3 (crosses).

distribution, e.g. $q = 11/6$ for the classical Dohnanyi case. See Sect. 4.3 for details.

3.3. *Dependence on Eccentricities of Parent Bodies*

The intrinsic collisional probability of planetesimals is nearly independent of their eccentricities, as long as they are not too high (see, e.g. Krivov et al. 2006). Nevertheless, eccentricities determine impact velocities and, through that, the minimum size of a disruptive projectile. Therefore, higher planetesimal eccentricities imply a larger rate of catastrophic collisions and thus a faster collisional evolution. To quantify the dependence, we have made runs with maximum eccentricities of 0.1, 0.2, 0.3, and 0.4 (Table 1) and determined the values of C. The results suggest a power law $C \propto e_{\max}^{9/4}$ as shown in Fig. 3.

This result comes as a surprise. Wyatt et al. (2007a) derive $C \propto e^{5/3}$. The same scaling is inherited by our analytic model, see Eq. (36) below. Since this discrepancy can be either due to an incompleteness of the analytic approach or to a non-linear relation between the maximum and the effective eccentricity, we tried to rule out the latter case by performing additional runs with e confined to narrow bins of width 0.1, centered at 0.05, 0.15, 0.25, and 0.35. These runs can be well described by the same power law, $C \propto e^{9/4}$ (Fig. 3). Therefore, the analytic model fails to reproduce this particular dependence. Nevertheless, it correctly describes many others, as the next sections will show.

4. ANALYTIC MODEL FOR EVOLUTION OF DISK MASS AND DUST MASS

4.1. *Size and Mass Distributions*

In what follows, we will analyze size or mass distributions of objects. Different authors use distributions of different physical quantities (number, cross section, mass) with different arguments (particles size or mass) and of different type (differential, cumulative, per size decade, etc.). A standard choice is to use a differential size distribution, $n(s)$, that gives the number of particles per unit size interval:

$$n(s) \equiv \int n(\mathbf{p}, s) \mathrm{d}\mathbf{p}, \tag{14}$$

or a differential mass distribution, $n(m)$, that gives the number of particles per unit mass interval. Instead of n, it is often convenient to use the mass-per-size-decade distribution,

$$\frac{\mathrm{d}M_{\mathrm{disk}}}{\mathrm{d}\log_{10} s} = \ln(10)\, s\, m(s)\, n(s). \tag{15}$$

In contrast to $n(s)$, this quantity tells us directly, objects in which size range contribute the most to the mass of the system. Therefore, we will use it when plotting size or mass distributions.

In the case of a power-law size distribution, $n(s)\mathrm{d}s \propto s^{2-3q}\mathrm{d}s$ is the number of objects with sizes $[s, s + \mathrm{d}s]$ and $n(m)\mathrm{d}m \propto m^{-q}\mathrm{d}m$ is the number of objects with masses $[m, m + \mathrm{d}m]$. The mass per size decade is $\propto s^{6-3q} \propto m^{2-q}$. When $q < 2$, the total mass is determined by large bodies, whereas the cross section is dominated by small particles as long as $q > 5/3$.

4.2. *Three-Slope Distribution*

The combination of material strength at smaller sizes and self-gravity at larger ones, with a turnover at around 100 m, causes the size distribution in a collisionally evolving system to strongly deviate from a single-slope power law, especially for object sizes of around 1 km. This is illustrated by Fig. 4 that shows how a disk evolves from the first-guess power law to a more realistic size distribution. The speed of this evolution is determined by the collisional timescales of populations of different-sized particles in the disk. Populations of smaller particles with sufficiently short lifetimes consist mostly of fragments of disruption of larger bodies. They will have reached collisional equilibrium with each other soon, according to their production rate by populations with longer lifetimes. Those latter populations of bigger particles will still be on their way to a steady state. As time goes by, more and more long-lived populations will undergo the transition from primordial to reprocessed material.

As this transitional mass moves towards larger objects with time, the smaller particles follow to a new "intermediate steady state". The lower panel of Fig. 4 shows the development of the characteristic wavy shape in the size distribution (e.g., Campo Bagatin et al. 1994; Thébault et al. 2003; Krivov et al. 2006) at the small-size end near the blowout limit due to radiation pressure. Once established, this shape remains constant. Only the absolute level changes because this distribution at smaller sizes acts as the trail of the distribution at larger

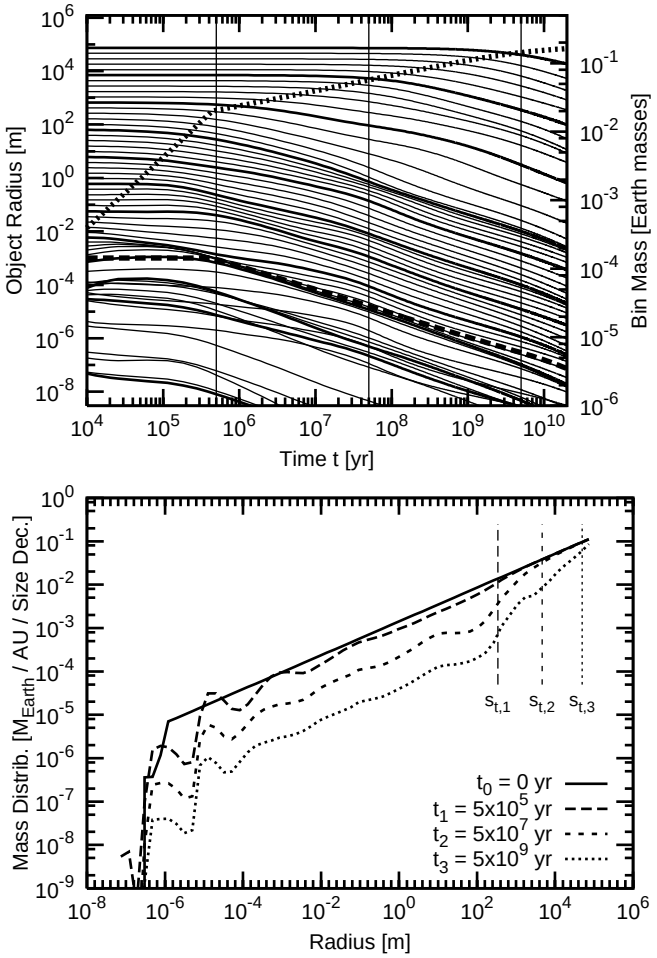


FIG. 4.— Results of the ii-0.3 run. *Top:* Time evolution of mass in individual mass bins, from the largest bodies of 74 km in radius to the smallest, 74 nm in radius. The mass ratio between adjacent bins is 4. Each solid line corresponds to one individual bin and gives the mass contained in that bin (see the right axis) as a function of time. The left axis can be used to find the line that corresponds to a given object size. The thick dashed curve corresponds to $\approx$ 1 mm radius, i.e. to the largest solids still treated as dust. The thick dotted curve, which goes roughly through the turning points of the curves, is the transition size $s_{\rm t}(t)$; see Eq. (37). *Bottom:* Size/mass distribution at four specific instants of time shown in the top panel with vertical lines: initially, after 5×10^5 years when $s_{\rm t}$ has reached $s_{\rm b}$, and after 5×10^7 and 5×10^9 yr when significant dust depletion has already occurred.

sizes. In the upper panel of Fig. 4, the number of smaller particles is constant for some time and then goes down, as soon as the distribution in the gravity regime starts to deviate from its primordial one.

These arguments suggest that an overall size distribution $n(s)$ can be approximated by a combination of three power laws (Fig. 5). For particles large enough to be only barely affected by collisions at time t, we assume n to follow $s^{2-3q_{\rm p}}$. Here, $q_{\rm p}$ is the "primordial" slope determined by the processes in which these planetesimals have formed. Small particles that are in quasi-steady state are separated from bigger primordial objects by a transition zone which we characterize by a time-dependent size $s_{\rm t}(t)$. To distinguish between the strength and gravity regimes, we introduce two more power laws and assume the mass distribution to follow $n \propto s^{2-3q_{\rm g}}$ for gravity-dominated quasi-steady state and $n \propto s^{2-3q_{\rm s}}$ for strength-dominated quasi-steady state. The two regimes are separated by an object size $s_{\rm b}$, which we will call breaking radius. Thus, the waviness is neglected, but the effect of a size-dependent $Q_{\rm D}^*$ is kept.

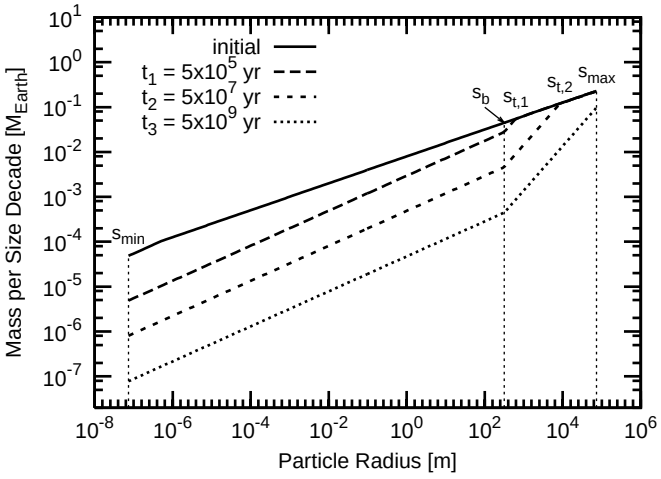


FIG. 5.— Schematic plot of the three regimes in the mass distribution and its time evolution. The mass $s_{\rm t}$ divides second generation material in collisional equilibrium ($s < s_{\rm t}$) from primordial material ($s > s_{\rm t}$), while $s_{\rm b}$ divides the material strength regime ($s < s_{\rm b}$) from the gravity regime ($s > s_{\rm b}$).

The resulting size distribution is given by

$$n(s) = n_{\rm max} \left(\frac{s_{\rm max}}{s} \right)^{3q_{\rm p}-2} \tag{16}$$

for $s_{\rm t} \leq s < s_{\rm max}$,

$$n(s) = n_{\rm max} \left(\frac{s_{\rm max}}{s_{\rm t}} \right)^{3q_{\rm p}-2} \left(\frac{s_{\rm t}}{s} \right)^{3q_{\rm g}-2} \tag{17}$$

for $s_{\rm b} \leq s < s_{\rm t}$, and

$$n(s) = n_{\rm max} \left(\frac{s_{\rm max}}{s_{\rm t}} \right)^{3q_{\rm p}-2} \left(\frac{s_{\rm t}}{s_{\rm b}} \right)^{3q_{\rm g}-2} \left(\frac{s_{\rm b}}{s} \right)^{3q_{\rm s}-2} \tag{18}$$

for $s_{\rm min} < s < s_{\rm b}$, where $n_{\rm max} \equiv n(s_{\rm max})$, with $s_{\rm max}$ being the size of the largest planetesimals. From this distribution, two important quantities can be derived. One is the total *disk* mass,

$$M_{\rm disk} = \int_{s_{\rm min}}^{s_{\rm max}} n(s) \frac{4}{3} \pi \rho s^3 {\rm d}s, \tag{19}$$

and the other is *dust* mass (that determines the infrared luminosity and therefore provides a link to observations),

$$M_{\rm dust} = \int_{s_{\rm min}}^{s_{\rm d}} n(s) \frac{4}{3} \pi \rho s^3 {\rm d}s, \tag{20}$$

where $s_{\rm min} \leq s_{\rm d} < s_{\rm b}$.

4.3. *Collisional Lifetimes of Planetesimals*

As seen from Eqs. (16)–(20), the evolution of $M_{\rm disk}$ and $M_{\rm dust}$ is controlled by $n_{\rm max}(t)$ and $s_{\rm t}(t)$.

We start with $n_{\rm max}$ and assume, according to Eqs. (2) and (9):

$$n_{\rm max}(t) = \frac{n_{\rm max}(0)}{1 + t/\tau_{\rm max}}, \tag{21}$$

where $\tau_{\rm max}$ is the collisional lifetime of these largest bodies. Equation (21) closely reproduces the disk evolution as soon as the whole system has reached the quasi-steady state at all sizes or, in other words, as soon as $s_{\rm t}(t)$ has reached $s_{\rm max}$.

The second quantity that we need, $s_{\rm t}(t)$, could easily be obtained by inverting the function $\tau(s)$, the collisional lifetime of planetesimals of a given size s. To obtain $\tau(s)$, we begin with the lifetime of the largest objects in a disk. Assuming that $q > 5/3$, Wyatt et al. (2007a, their Eq. 12) approximated it as

$$\tau_{\rm max} = \frac{4\pi}{\sigma_{\rm tot}} \cdot \left(\frac{s_{\rm max}}{s_{\rm min}}\right)^{3q_{\rm p}-5} \cdot \frac{r^{5/2}{\rm d}r}{(\mathsf{G}M_*)^{1/2}} \times \frac{I}{f(e,I)G(q,s)}. \quad (22)$$

where e and I are the effective orbital eccentricities and inclinations, $\sigma_{\rm tot}$ is the initial cross sectional area of the disk material, G the gravitational constant, r the radial distance of the ring of parent bodies, and ${\rm d}r$ its width. The slope q in their single-power-law approach corresponds to the primordial slope $q_{\rm p}$ in our nomenclature. The functions f and G are given by

$$f(e,I) = \sqrt{\frac{5}{4}e^2 + I^2}, \quad (23)$$

$$G(q,s) = \left[X_{\rm c}(s)^{5-3q} - \left(\frac{s_{\rm max}}{s}\right)^{5-3q}\right] + 2\frac{q-5/3}{q-4/3}\left[X_{\rm c}(s)^{4-3q} - \left(\frac{s_{\rm max}}{s}\right)^{4-3q}\right] + \frac{q-5/3}{q-1}\left[X_{\rm c}(s)^{3-3q} - \left(\frac{s_{\rm max}}{s}\right)^{3-3q}\right], \quad (24)$$

with

$$X_{\rm c}(s) = \left(\frac{2Q^*_{\rm D}(s)\, r f(e,I)^{-2}}{\mathsf{G}M_*}\right)^{1/3}. \quad (25)$$

While $f(e,I)$ describes the dependence of the impact velocities on eccentricities and inclinations, the functions G and $X_{\rm c}$ characterize the disruption of planetesimals by smaller projectiles. Namely, $X_{\rm c}(s)$ is the minimum size ratio between the smallest disruptive projectile and the target, and $G(q,s)$ is the number of disruptive projectiles.

We need the lifetime of objects of an arbitrary size, $\tau(s < s_{\rm max})$. To derive it, we can simply substitute $s_{\rm max}$ by s in Eq. (22), obtaining

$$\tau(s) = \frac{4\pi}{\sigma_{\rm tot}} \cdot \left(\frac{s}{s_{\rm min}}\right)^{3q_{\rm p}-5} \cdot \frac{r^{5/2}{\rm d}r}{(\mathsf{G}M_*)^{1/2}} \times \frac{I}{fG(q_{\rm p},s)}. \quad (26)$$

In order to replace the dependence on the initial cross sectional area of objects, $\sigma_{\rm tot}$, with their initial total mass, M_0, we need to derive both quantities from the initial size distribution in Eq. (16). The area is given by

$$\sigma_{\rm tot} = n_{\rm max}(0) \cdot \frac{\pi s^3_{\rm max}}{3q_{\rm p}-5}\left[\left(\frac{s_{\rm max}}{s_{\rm min}}\right)^{3q_{\rm p}-5} - 1\right]. \quad (27)$$

Since it is dominated by $s_{\rm min}$ for $q_{\rm p} > 5/3$, we obtain

$$\sigma_{\rm tot} = n_{\rm max}(0) \cdot \frac{\pi s^3_{\rm max}}{3q_{\rm p}-5}\left(\frac{s_{\rm max}}{s_{\rm min}}\right)^{3q_{\rm p}-5}. \quad (28)$$

The initial total disk mass is

$$M_0 = n_{\rm max}(0) \cdot \frac{4\pi\rho s^4_{\rm max}}{3(6-3q_{\rm p})}\left[1 - \left(\frac{s_{\rm min}}{s_{\rm max}}\right)^{6-3q_{\rm p}}\right]. \quad (29)$$

For $q_{\rm p} < 2$, it is dominated by $s_{\rm max}$. However, since a primordial slope $q_{\rm p} \geq 2$ is not unrealistic (see Sect. 4.8) we refrain from using a further approximation. Then, the area and the mass are related through

$$\sigma_{\rm tot} = M_0 \cdot \frac{3(2-q_{\rm p})}{4(q_{\rm p}-5/3)} \cdot s^{-1}_{\rm max} \cdot \left(\frac{s_{\rm max}}{s_{\rm min}}\right)^{3q_{\rm p}-5} \times \left[1 - \left(\frac{s_{\rm min}}{s_{\rm max}}\right)^{6-3q_{\rm p}}\right]^{-1}. \quad (30)$$

Inserting Eq. (30) into Eq. (26) results in

$$\tau(s) = \frac{16\pi\rho}{3M_0} \cdot \left(\frac{s}{s_{\rm max}}\right)^{3q_{\rm p}-5} \frac{s_{\rm max} r^{5/2}{\rm d}r}{(\mathsf{G}M_*)^{1/2}} \times \frac{q_{\rm p}-5/3}{2-q_{\rm p}}\left[1 - \left(\frac{s_{\rm min}}{s_{\rm max}}\right)^{6-3q_{\rm p}}\right] \times \frac{I}{f(e,I)G(q_{\rm p},s)}, \quad (31)$$

which gives the collisional lifetime of an object with radius s. Note that

$$\frac{1}{2-q_{\rm p}}\left[1 - \left(\frac{s_{\rm min}}{s_{\rm max}}\right)^{6-3q_{\rm p}}\right] \longrightarrow 3\ \ln\frac{s_{\rm max}}{s_{\rm min}} \quad (32)$$

for $q_{\rm p} \rightarrow 2$.

If the mean impact velocities in the system are high enough to allow planetesimals of radius s to get disrupted in a collision, i.e. $X_{\rm c}(s) \ll s_{\rm max}/s$, $G(q_{\rm p},s)$ reduces to

$$G(q_{\rm p},s) \approx \frac{q_{\rm p}-5/3}{q_{\rm p}-1} \cdot X_{\rm c}(s)^{3-3q_{\rm p}}, \quad (33)$$

and $\tau(s)$ to

$$\tau(s) = \frac{16\pi\rho}{3M_0} \cdot \left(\frac{s}{s_{\rm max}}\right)^{3q_{\rm p}-5} \cdot r^2{\rm d}r \cdot \left(\frac{r}{\mathsf{G}M_*}\right)^{q_{\rm p}-1/2} \times \frac{q_{\rm p}-1}{2-q_{\rm p}}\left[1 - \left(\frac{s_{\rm min}}{s_{\rm max}}\right)^{6-3q_{\rm p}}\right] \cdot (2Q^*_{\rm D})^{q_{\rm p}-1} \times \frac{I}{f(e,I)^{2q_{\rm p}-1}} \quad (34)$$

Now, we take into account the dependence of $Q^*_{\rm D}$ on the object size s, as was done by O'Brien & Greenberg (2003). If we are only interested in the gravity regime, $s > s_{\rm b}$, Eq. (1) is simplified to

$$Q^*_{\rm D}(s) \approx Q^*_{\rm D,b} \cdot \left(\frac{s}{s_{\rm b}}\right)^{3b_{\rm g}}, \quad (35)$$

where $Q^*_{\rm D,b}$ is the critical specific energy at the breaking radius, i.e. around the minimum of $Q^*_{\rm D}(s)$. Assuming, further, that $I \propto e$, we can write down the dependencies of the collisional lifetime,

$$\tau(s) \propto \sigma^{-1}_{\rm tot} \cdot s^{3q_{\rm p}-5+3(q_{\rm p}-1)b_{\rm g}} \cdot r^{3/2+q_{\rm p}} \cdot {\rm d}r \cdot e^{-5/3}. \quad (36)$$

O'Brien & Greenberg (2003) yield the same size dependence on s in their Eq. (11).

To find $s_{\rm t}(t)$, the object size below which a steady state is reached, we assume that the populations move from their primordial state to the quasi-steady state instantaneously when

the system age reaches their initial mean collisional lifetime, $\tau(s_{\rm t}) = t$. Inverting that, the resulting mass of objects in transition can be retrieved as a function of system age. Keeping the assumption $X_{\rm c} \ll s_{\rm max}/s$, the relation is

$$s_{\rm t}(t) \propto t^{1/(3q_{\rm p}-5+3(q_{\rm p}-1)b_{\rm g})} \tag{37}$$

for $t > \tau(s_{\rm b}) \equiv \tau_{\rm b}$. This transitional size is also plotted in Fig. 4.

Pan & Sari (2005) followed a similar approach in their study of the Kuiper-belt size distribution. Describing the propagation of the shock wave through the target, they introduce a parameter β that varies between $3/2$ (if all energy of a projectile goes to the shock wave) and 3 (if all its momentum does). Their β equals $1/b_{\rm g}$ in our nomenclature, and $b_{\rm g} = 0.5$ leads to $\beta = 2$. Additionally, we have to replace their slope q_0 with our $3q_{\rm p} - 2$. Then, given their Eqs. (6), (7), and $N_{>s} \propto s^{3-3q_{\rm p}}$, we yield the same exponent as in our Eq. (37). Note that what Pan & Sari (2005) call "breaking radius" is our "transition radius" $s_{\rm t}$, and their "radius of equilibrium" is our "breaking radius" $s_{\rm b}$.

4.4. *Evolution of Disk Mass*

Now, we derive the full expression for the time-dependent total disk mass. Using the size distribution given by Eq. (18), $n_{\rm max}$ from Eq. (21) and expressing $n_{\rm max}(0)$ through M_0 with the aid of Eq. (29), we can perform the integration in Eq. (19). Then, the resulting time-dependent disk mass is

$$\begin{aligned} M_{\rm disk}(t) = & \frac{M_0}{1+t/\tau_{\rm max}} \left[1 - \left(\frac{s_{\rm min}}{s_{\rm max}}\right)^{6-3q_{\rm p}}\right]^{-1} \\ & \times \left[1 - \left(\frac{s_{\rm t}(t)}{s_{\rm b}}\right)^{6-3q_{\rm p}} \left(\frac{s_{\rm b}}{s_{\rm max}}\right)^{6-3q_{\rm p}} \left(1 - \frac{2-q_{\rm p}}{2-q_{\rm g}}\right)\right. \\ & + \left(\frac{s_{\rm t}(t)}{s_{\rm b}}\right)^{3q_{\rm g}-3q_{\rm p}} \left(\frac{s_{\rm b}}{s_{\rm max}}\right)^{6-3q_{\rm p}} \left(\frac{2-q_{\rm p}}{2-q_{\rm s}} - \frac{2-q_{\rm p}}{2-q_{\rm g}}\right) \\ & - \left(\frac{s_{\rm t}(t)}{s_{\rm b}}\right)^{3q_{\rm g}-3q_{\rm p}} \left(\frac{s_{\rm b}}{s_{\rm max}}\right)^{3q_{\rm s}-3q_{\rm p}} \left(\frac{s_{\rm min}}{s_{\rm max}}\right)^{6-3q_{\rm s}} \\ & \left. \times \left(\frac{2-q_{\rm p}}{2-q_{\rm s}}\right)\right] \end{aligned} \tag{38}$$

for $\tau_{\rm b} < t < \tau_{\rm max}$. To make Eq. (38) valid for earlier phases, i.e. for $t < \tau_{\rm b}$, $s_{\rm b}$ should be replaced by $s_{\rm t}(t)$. The sizes involved are the maximum object size $s_{\rm max}$, the transition size between the primordial and reprocessed material $s_{\rm t}$, the breaking radius between the gravity and strength regime $s_{\rm b}$. The lower limit in the size distribution, $s_{\rm min}$, is crucial for the dust emission and it is usually taken to be the radiation pressure blowout limit. As long as $q_{\rm p} < 2$, it is fairly unimportant for the mass budget. However, we are interested in $q_{\rm p} \geq 2$ as well. Therefore, we can safely set $s_{\rm min} = 0$ only in the last line of Eq. (38), where it enters through $s_{\rm min}/s_{\rm max}$ to the power of $6 - 3q_{\rm s}$, with $q_{\rm s} \approx 11/6 < 2$.

The relative importance of the terms in Eq. (38) is illustrated in Fig. 6. A combination of the classic Dominik-Decin behavior in the first line of Eq. (38) together with the second line is a reasonably accurate approximation to $M_{\rm disk}(t)$ for most of the time. With the aid of Eq. (37), Eq. (38) transforms to

$$\begin{aligned} M_{\rm disk}(t) \approx & \frac{M_0}{1+t/\tau_{\rm max}} \left[1 - \left(\frac{s_{\rm min}}{s_{\rm max}}\right)^{6-3q_{\rm p}}\right]^{-1} \\ & \times \left[1 - \left(\frac{s_{\rm b}}{s_{\rm max}}\right)^{6-3q_{\rm p}} \cdot \left(\frac{t}{\tau_{\rm b}}\right)^{\frac{2-q_{\rm p}}{q_{\rm p}-5/3+(q_{\rm p}-1)b_{\rm g}}}\right. \end{aligned}$$

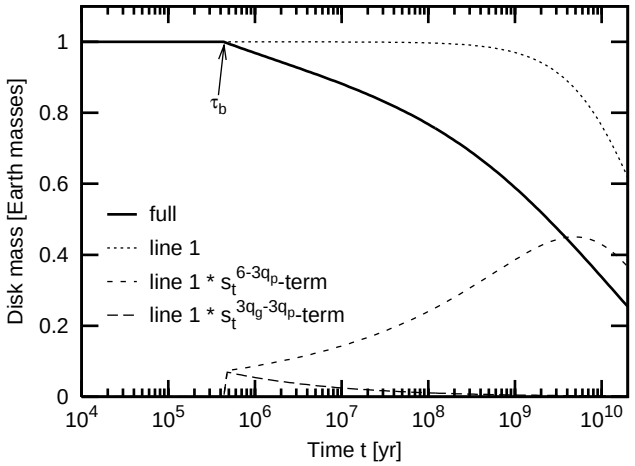


FIG. 6.— The contributions of different terms in Eq. (38) (dotted and dashed lines) and their total (solid line).

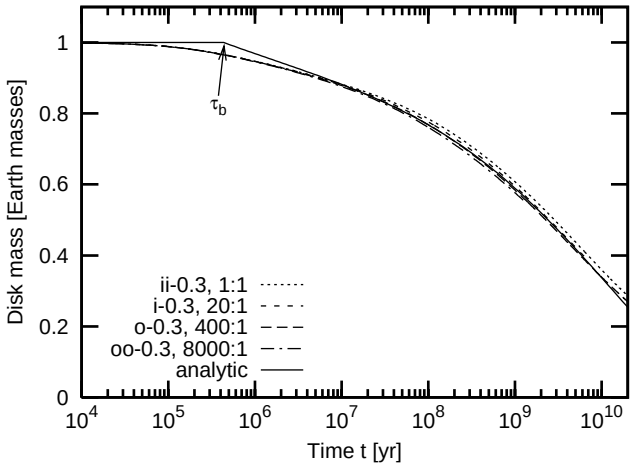


FIG. 7.— Evolution of total masses with (scaled) time, obtained in four numerical runs and with the analytic model.

$$\left. \times \left(1 - \frac{2-q_{\rm p}}{2-q_{\rm g}}\right)\right] \tag{39}$$

for $\tau_{\rm b} < t < \tau_{\rm max}$. At $t \ll \tau_{\rm max}$, and assuming $q_{\rm p} = 1.87$, a further approximation is

$$M_{\rm disk}(t) \approx M_0 \left(1 - {\rm const} \cdot t^{0.2}\right). \tag{40}$$

The evolution of the disk mass, both from the numerical runs and from the analytic solution (38), is plotted in Fig. 7, showing a good agreement between analytics and numerics. A deviation is only seen around $t = \tau_{\rm b}$ where the transition from primordial to reprocessed state sets on for gravity-dominated objects. The reason is that, to ease the analytic treatment, we neglect the smooth natural transition from material strength to self-gravity given by Eq. (1) and assume a sharp break between the two power laws instead.

4.5. *Evolution of Disk Mass at Latest Stages*

As soon as the age of the system has reached the collisional lifetime of the largest bodies, i.e. at $t > \tau_{\rm max}$, the solids of all sizes in the disk reach quasi-steady state, and the change in total mass will be dominated by $1/t$. At this latest phase, the

projectiles that can destroy objects of size $s_{\rm max}$ no longer follow a size distribution with the primordial slope, $2-3q_{\rm p}$. Instead, they have the slope of a collisional cascade under gravity regime, $2-3q_{\rm g}$. The slightly longer collisional lifetime can neither be expressed through Eq. (22) that uses the *initial* cross section $\sigma_{\rm tot}$ nor through Eq. (31) that contains the initial disk mass M_0 and slope $q_{\rm p}$. The correct way to evaluate $\tau_{\rm max}$ is to use the initial number density of biggest objects, $n_{\rm max}(0)$, and the slope $q_{\rm g}$. Expressing $\sigma_{\rm tot}$ in Eq. (22) through $n_{\rm max}$ with the help of Eq. (28) and replacing then $q_{\rm p}$ with $q_{\rm g}$, we obtain

$$\tau_{\rm max} = \frac{12q_{\rm g}-20}{n_{\rm max}(0)\cdot s_{\rm max}^3}\cdot\frac{r^{5/2}{\rm d}r}{({\rm G}M_*)^{1/2}} \times\frac{I}{f(e,I)G(q_{\rm g},s_{\rm max})}. \quad (41)$$

Expressing now $n_{\rm max}(0)$ through M_0 by virtue of Eq. (29) yields

$$\tau_{\rm max} = \frac{16\pi\rho}{3M_0}\cdot s_{\rm max}\cdot\frac{r^{5/2}{\rm d}r}{({\rm G}M_*)^{1/2}} \times\frac{q_{\rm g}-5/3}{2-q_{\rm p}}\left[1-\left(\frac{s_{\rm min}}{s_{\rm max}}\right)^{6-3q_{\rm p}}\right]^{-1} \times\frac{I}{f(e,I)G(q_{\rm g},s_{\rm max})}, \quad (42)$$

where both slopes, $q_{\rm p}$ and $q_{\rm g}$, appear (cf. Eqs. 22 and 31).

4.6. *Evolution of Mass in Dynamically "Cold" Disks*

All the treatment above applies to planetesimal belts where relative velocities are high enough for the biggest objects to be destroyed by mutual collisions. This might not be the case in dynamically "cold" disks with low eccentricities and inclinations and/or very far from the star.

Consider again the lifetime of objects $\tau(s)$. As s increases, $X_{\rm c}(s)$ (Eq. 25) increases too and at a certain point reaches $s_{\rm max}/s$. At this point, G (Eq. 24) becomes zero and $\tau(s)$ (Eq. 31) goes to infinity. This means that, for a given impact velocity, objects above a certain critical size cannot be disrupted anymore. In systems with low relative velocities, that critical size may happen to be smaller than $s_{\rm max}$. This will affect the mass evolution. Specifically, when $s_{\rm t}$ reaches that critical size, the overall mass decay ceases.

To illustrate such effects, Fig. 8 shows the influence of the effective e and I on the evolution of the total mass of a disk of initially 1 $M_\oplus$ at an effective distance of 10 AU, calculated with our analytic model. For colder disks, the curves start to flatten. This happens because the largest planetesimals (that dominate the total mass) stay intact, which slows down the mass loss.

4.7. *Evolution of Dust Mass*

The dust mass can be evaluated in a similar way as the disk mass. We use now Eqs. (18), (20), (21), (29), and (37). Neglecting the minimum mass $s_{\rm min}$ only when it enters the formula through $s_{\rm min}/s_{\rm max}$, we obtain

$$M_{\rm dust}(t) = \frac{M_0}{1+t/\tau_{\rm max}}\cdot\left(\frac{t}{\tau_{\rm b}}\right)^{\frac{q_{\rm g}-q_{\rm p}}{q_{\rm p}-5/3+(q_{\rm p}-1)b_{\rm g}}}\cdot\frac{2-q_{\rm p}}{2-q_{\rm s}} \times\left(\frac{s_{\rm b}}{s_{\rm max}}\right)^{2-q_{\rm p}}\left[\left(\frac{s_{\rm d}}{s_{\rm b}}\right)^{2-q_{\rm s}}-\left(\frac{s_{\rm min}}{s_{\rm b}}\right)^{2-q_{\rm s}}\right]^{-1} \quad (43)$$

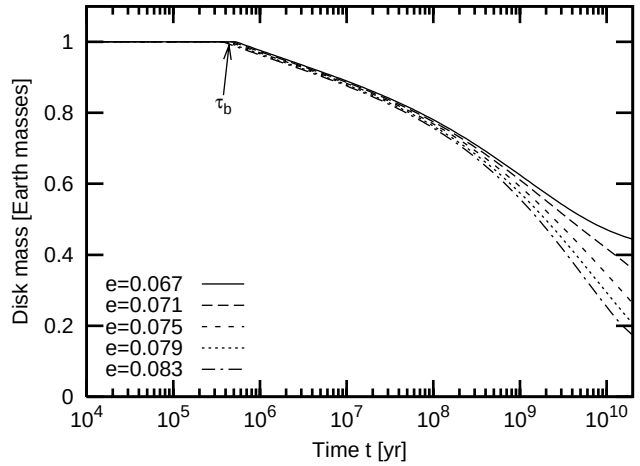


FIG. 8.— Influence of the effective eccentricity assumed in the analytic model for a disk of 1 $M_\oplus$ at $r=10$ AU with a radial extent ${\rm d}r=7.5$ AU. The $I=e/2$ relation between eccentricity and inclination is assumed.

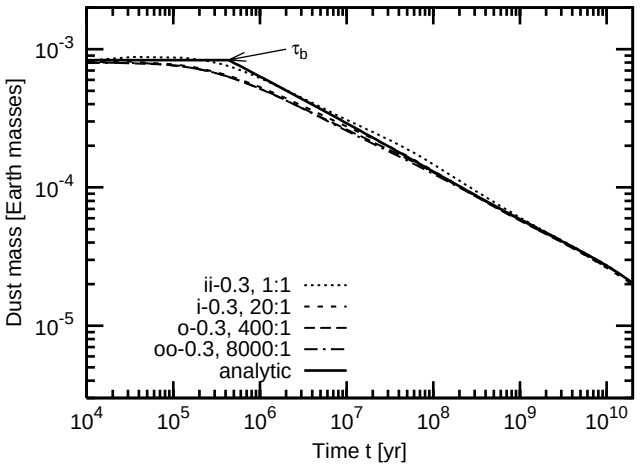


FIG. 9.— Similar to Fig. 7 but for dust masses, i.e. masses in particles with radii below 1 mm.

for $\tau_{\rm b}<t<\tau_{\rm max}$. Before that, i.e. at $t<\tau_{\rm b}$, we have $q_{\rm s}$ and $b_{\rm s}$ instead of $q_{\rm g}$ and $b_{\rm g}$, respectively. If the assumed primordial slope, $q_{\rm p}$, equals the steady-state slope in the strength regime, $q_{\rm s}$, the dust mass stays constant, which is the case for the first part of the numerical integration. However, as soon as the transitional zone reaches objects large enough to be influenced by self-gravity, Eq. (43) starts to work. It shows that the evolution of dust mass depends most strongly on the difference between $q_{\rm p}$ and $q_{\rm g}$. The dust mass decay, obtained both from the numerical runs and analytic solution (43), are shown in Fig. 9. For $t>\tau_{\rm b}$, we roughly have $M_{\rm dust}\propto t^\xi$ with $\xi\approx-0.3$.

We finally note that Eq. (43) is valid as long as the collisional lifetime of the largest planetesimals is longer than the age of the system. When $t>\tau_{\rm max}$, $t/\tau_{\rm b}$ in that equation must be replaced by $\tau_{\rm max}/\tau_{\rm b}$.

4.8. *The Model Parameters*

Our analytic model contains several parameters that either differ from similar parameters in the numerical model (such as e) or are absent there (such as $q_{\rm s}$ and $q_{\rm g}$). To use the analytic model, we have to specify them. We now describe how

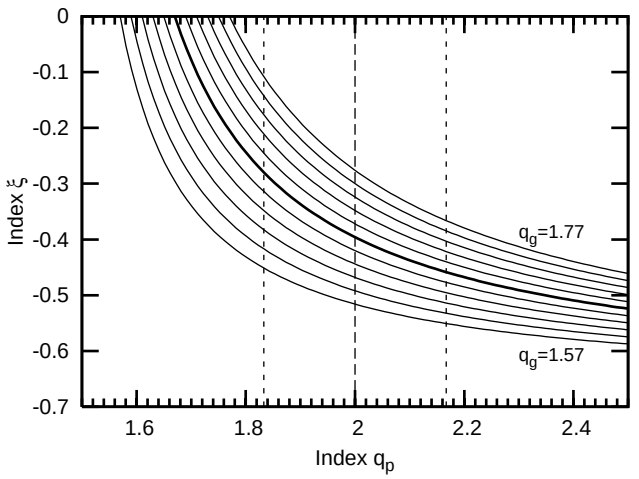


FIG. 10.— Index ξ of the power-law evolution of the dust mass, $M_{\rm d} \propto t^{\xi}$. The horizontal axis gives the dependence on the slope of the primordial mass distribution, $q_{\rm p}$, for values from $q_{\rm g} = 1.57$ (bottom) to $q_{\rm g} = 1.77$ (top) for the slope in the gravity regime. The bold line is for $q_{\rm g} = 1.67 \approx 5/3$. Vertical lines indicate the mean value and error estimates for $q_{\rm p}$ from Trujillo et al. (2001).

this can be done, explaining, in particular, the choice of parameters used to plot analytic curves in Figs. 6–9.

Two important free parameters of the analytic model are $q_{\rm s}$ and $q_{\rm g}$. We use the work of O'Brien & Greenberg (2003) who found the slope of the size distribution in a system in a collisional steady state. With the dependence of the critical specific energy on the object size given in Eq. (1), they give a power-law index

$$q = \frac{11/6 + b}{1 + b} \tag{44}$$

in their Eq. (24). With $b = b_{\rm s} = -0.1$ for the strength regime we have $q = q_{\rm s} = 1.877$. Similarly, with $b = b_{\rm g} = 0.5$ for the gravity regime, Eq. (44) can be used to derive $q_{\rm g} \approx 5/3$. It is these values that we used in Eq. (38) to produce Figs. 6–8 and in Eq. (43) to plot Fig. 9.

In contrast to $q_{\rm s}$ and $q_{\rm g}$, the primordial slope, $q_{\rm p}$, is a free parameter not only in the analytic model, but also in the numerical one. As stated in Sect. 2.4, in all "nominal" runs we assumed $q_{\rm p} = 1.87$, which corresponds to $p_{\rm p} = 3q_{\rm p} - 2 = 3.61$ in the size scaling. In principle, $q_{\rm p}$ describes the mass distribution at the onset of the collisional grinding of the disk and, therefore, represents a link to the planetesimal formation process. The outcome of the agglomeration phase is the input to the phase of disruptive collisions. The Kuiper belt is the only source for observational constraints to this parameter so far, and recent surveys suggest a value of $p_{\rm p} = 4.0 \pm 0.5$ (e.g., Trujillo et al. 2001; Bernstein et al. 2004) or $q_{\rm p} = 2.00 \pm 0.17$. Simulations by Kenyon & Bromley (2004) yield $p_{\rm p} = 4.0$–4.5 or $q_{\rm p} = 2.00$–2.17. According to Eq. (43), where we have $M_{\rm dust} \propto t^{\xi}$, and together with $q_{\rm g} \approx 1.67$, this would change the dust mass evolution from $M_{\rm dust} \propto t^{-0.32}$ for $q_{\rm p} = 1.87$ to $M_{\rm dust} \propto t^{-0.40}$ for $q_{\rm p} = 2.00$. Fig. 10 shows the rather moderate dependence of the index ξ on the two mass distribution slopes, $q_{\rm g}$ and $q_{\rm p}$.

While the dust size limit, $s_{\rm d}$, has little influence on the mass budget, the breaking size, $s_{\rm b}$, the maximum size, $s_{\rm max}$, and the ratio of the two are relevant to the evolution as they define the lifetime of the largest bodies $\tau_{\rm max}$ relative to $\tau_{\rm b}$. What is more, the ratio $s_{\rm b}/s_{\rm max}$ determines the rate of the mass decay in Eq. (39). From Sect. 2.2 we know the location of the breaking radius to be 316 m for the material properties assumed, and the upper size limit of all the runs was set to $s_{\rm max} = 74$ km.

Another parameter in the analytic model is the collisional lifetime of objects of breaking radius, $\tau_{\rm b} = \tau(m_{\rm b})$. Eq. (31) expresses it through other parameters critical for the efficiency of collisions: the radial distance to the star r, the disk radial extension $\mathrm{d}r$, and the effective eccentricity e and inclination I. We choose to fix both the effective distance and the disk extension to be $r = 4/3\mathrm{d}r = 10$ AU when reproducing analytically the results of the ii-0.3 run, 20 AU for i-0.3, 40 AU for o-0.3, and 80 AU for oo-0.3. Further, the inclination can be coupled to eccentricity by assuming the equilibrium condition $I = e/2$. Thus, only e remains as a free parameter. The best fit to, e.g., the ii-0.3 run is achieved if we assume $e \approx 0.075$ in the analytic model, which is approximately one quarter of $e_{\rm max} = 0.3$. With these choices, we find $\tau(s_{\rm b}) \approx 4 \times 10^5$ years.

Alternatively, $\tau_{\rm b}$ can be directly retrieved from the break in the evolution of the dust mass (see Fig. 9). This method gives $\tau(s_{\rm b}) \approx 5 \times 10^5$ years, which is approximately $4/3$ times the value calculated with Eq. (31). This discrepancy is probably a result of the particle-in-a-box assumptions made by Wyatt et al. (2007a) in derivation of Eq. (22). We prefer this empirical scaling and thus applied the factor of $4/3$ to all analytically estimated timescales in this paper.

5. EVOLUTION OF DISK LUMINOSITY

5.1. *Fractional Luminosity for a Given Age*

Following Wyatt et al. (2007a), we define the fractional luminosity of dust as

$$f_{\rm d} \equiv \sigma_{\rm tot}/(4\pi r^2), \tag{45}$$

which assumes that dust grains are black bodies, absorbing and re-emitting all the radiation they intercept. Wyatt et al. (2007a, their Eq. 20) found that there is a maximum possible fractional luminosity $f_{\rm max}$ for a given age, whose value is independent of the initial disk mass, but depends on other model parameters such as the distance r of the disk center from the star, its width $\mathrm{d}r$, size of the largest planetesimals $D_{\rm c}$, critical fragmentation energy $Q_{\rm D}^*$, orbital eccentricity of planetesimals e (with their inclination being $I = e/2$), as well as the stellar mass M_* and luminosity L_*.

We now wish to explore $f_d(t)$ and check whether it has an upper limit in the framework of our analytic model. To this end, we used Eq. (45) and calculated $\sigma_{\rm tot}$ with the aid of our Eq. (43) for the dust mass. We assumed a solar-type star with $M_* = L_* = 1$ and probed disks with $M_{\rm disk} = 1, 3, 10$, and $30 M_\oplus$; $r = 3, 10, 30$, and 100 AU; $\mathrm{d}r/r = 1/8, 1/4, 1/2$, and 1; $e = 0.05, 0.10, 0.15$, and 0.20. The results are presented in Fig. 11 (thick lines). As a standard case, we adopted $M_{\rm disk} = 10 M_\oplus$, $r = 30$ AU, $\mathrm{d}r/r = 1/2$, and $e = 0.10$. It is shown with a thick solid curve in each of the panels.

In the same Fig. 11, we have overplotted with thin lines the dust luminosity $f_{\rm d}$ computed with Eqs. (14), (19), and (20) of Wyatt et al. (2007a), for comparison. In that calculation, we assumed $Q_{\rm D}^* = 300$ J/kg (constant in their model), $D_{\rm c} = 60$ km, and the same values of those parameters that are common in their and our model (M_*, L_*, r, $\mathrm{d}r/r$, and e).

Analysis of Fig. 11 allows us to make a number of conclusions. First, as expected, our model yields more gently sloping curves than that by Wyatt et al. As discussed above, the $1/t$ law will be asymptotically reached in our model, too,

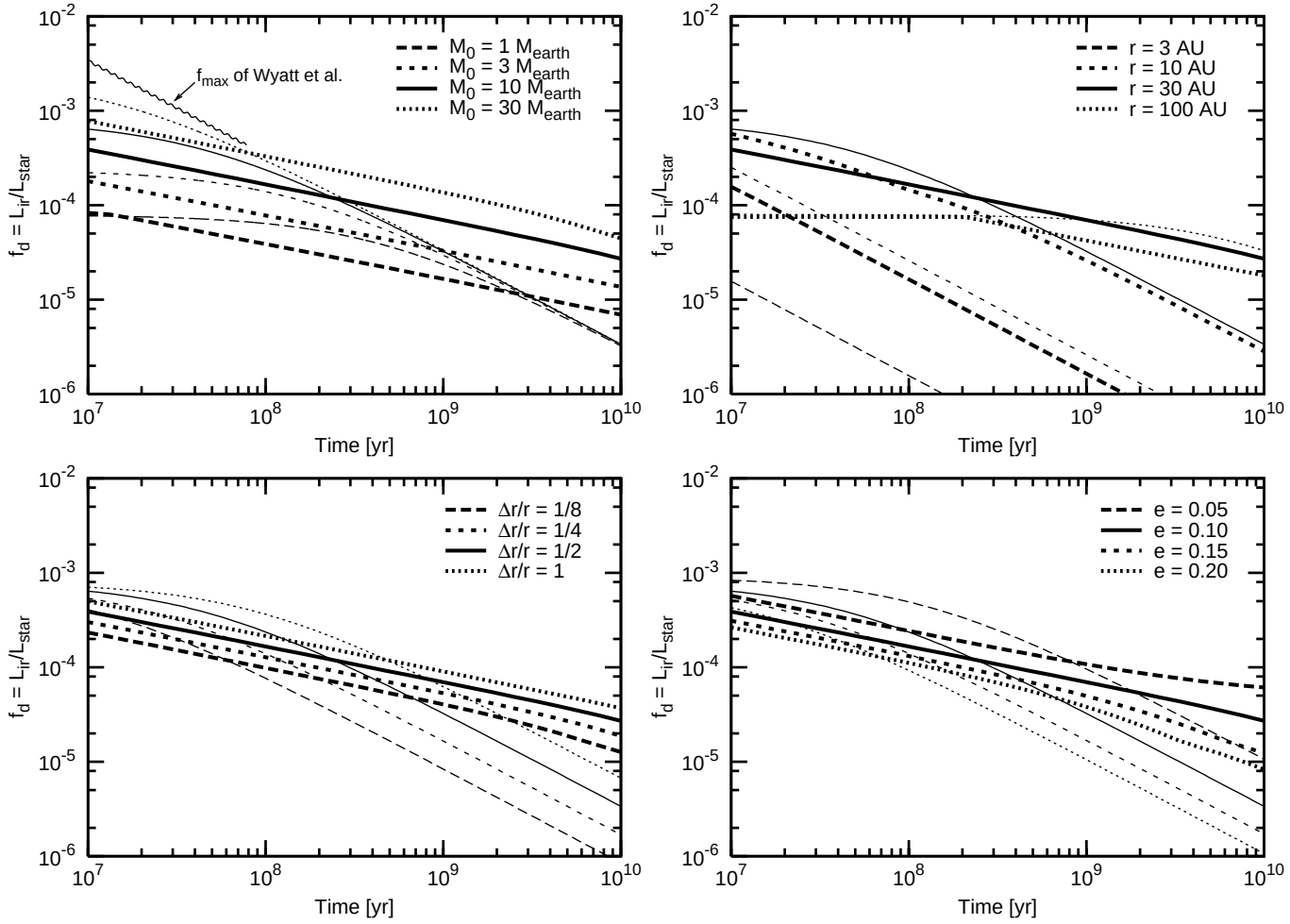


FIG. 11.— Fractional luminosity of dust around a solar-like star as a function of age. Thick lines: our analytic model; thin lines: $f_{\rm d}$ of Wyatt et al. (2007a). Different panels demonstrate dependence on different parameters: $M_{\rm disk}$ *(top left)*, r *(top right)*, ${\rm d}r/r$ *(bottom left)*, and e *(bottom right)*. A standard case with $M_* = L_* = 1$, $M_{\rm disk} = 10 M_\oplus$, $r = 30$ AU, ${\rm d}r/r = 1/2$, and $e = 0.10$ is shown with solid lines (common in all panels).

but this does rarely happen at ages $t < 10$ Gyr. Only the first signs of the curves' steepening appear at Gyr ages, and that only for the cases when the collisional evolution is faster (higher masses, closer-in or more confined dust rings, higher eccentricities). As a consequence of the slope difference between the two models, our model places more stringent upper limits of $f_{\rm d}$ at earlier ages, and conversely, it allows the Gyr-old systems to have a somewhat higher $f_{\rm d}$ than the model by Wyatt et al. does.

Next, the dependence of $f_{\rm max}$ on the initial disk mass, which cancels out in their model, is retained in our nominal runs (the top left panel). In fact, the maximum possible $f_{\rm d}$ is then determined by the maximum initial disk mass that still appears physically plausible in the framework of theories of planetesimal accretion and planet formation.

Another point to mention is that, whereas the dependence on the disk width (bottom right) and planetesimal eccentricities is relatively weak and monotonic, the dependence on the disk location (top right) is rather strong and more intricate. That the dependence is strong is the consequence of Eq. (13) that predicts the timescales to very sensitively depend on the distance from the star, and of Eq. (45) that contains a "dilution factor" r^2. At the beginning of the evolution, the innermost ring is always the brightest because the dilution factor r^2 in Eq. (45) is the smallest. At the end of the evolution, the opposite is true: the outermost ring will become the brightest, because its collisional evolution is the slowest and it retains more mass than inner disks. Therefore, all four curves intersect each other at a certain point; the 30 and 100 AU curve do that after 10 Gyr, i.e. outside that right edge of the plot. After that, all the curves go parallel to each other in the "Dominik-Decin regime", following a $1/t$ law. Note that inner rings reach the $1/t$ regime more quickly: already at 10 AU it is established in around 100 Myr for an initial mass of 10 $M_\oplus$.

Although the existence of a "maximum fractional luminosity for a given age", as suggested by Wyatt et al. (2007a), no longer holds in our model as a robust mathematical statement, in practice our model still suggests that $f_{\rm d}(t)$ cannot exceed a certain limit, unless the model parameters take extreme values, incompatible with our understanding of the planetesimal disks. For instance, we do expect $f_{\rm d} < 10^{-4}$ at $t = 10$ Gyr, provided that the initial disk did not contain more than 30 earth masses of solids and that the mean orbital eccentricity of planetesimals is not lower than 0.1 (corresponding to the mean inclination larger than 3°). Therefore, plots such as Fig. 11 can be used to check whether or not $f_{\rm d}$ observed for a certain system with a known age is compatible with a "smooth", unperturbed collisional evolutionary scenario. In case it is not, it will be an indication that other mechanisms (delayed stirring, recent giant break-ups, non-collisional dust

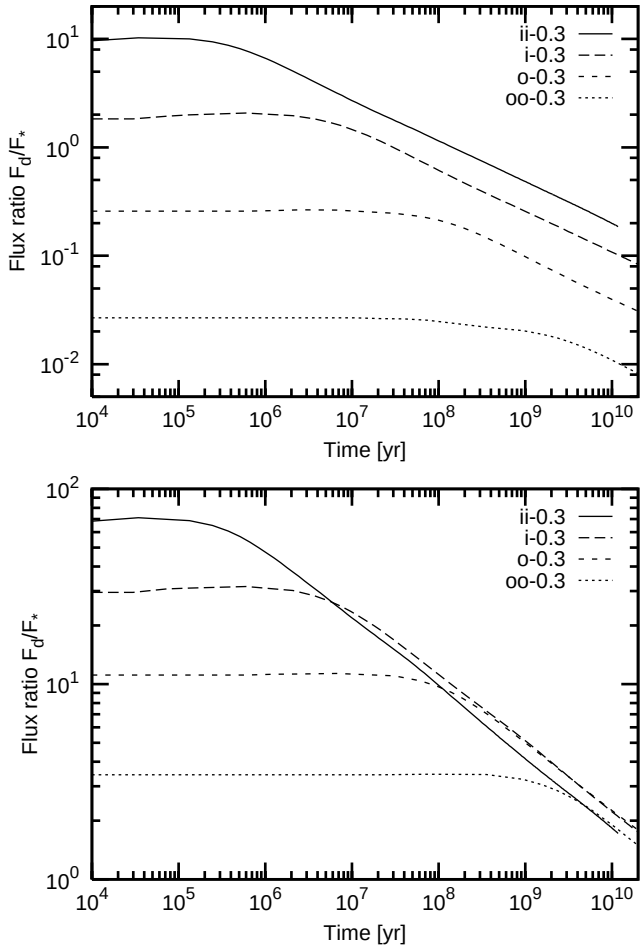


FIG. 12.— Flux ratio versus time for *(top)* 24 μm and *(bottom)* 70 μm.

production etc.) should be thought of to explain the observations.

5.2. *24 and 70 Micron Fluxes from Partial Rings*

In order to produce directly observable quantities from the derived dust masses, we now concentrate on dust luminosities at particular infrared wavelengths. We calculated the dust temperature and the thermal emission integrated over the whole disk with a more accurate, yet sufficiently simple, model, assuming that the absorption/emission efficiency is constant up to wavelengths of 2π times the size of the particles, s, and proportional to s^{-1} beyond that (Backman & Paresce 1993). Then we computed the spectral flux densities of dust emission $F_{\rm d}$ and of the stellar radiation F_* at a certain wavelength, as well as their ratio $F_{\rm d}/F_*$. As the size distribution in the dust regime quickly reaches its steady state, the luminosity $F_{\rm d}$ is directly proportional to the dust mass. Therefore, the same initial constancy and subsequent t^ξ decay with $\xi = -0.3 \ldots -0.4$ apply.

Fig. 12 shows the evolution of the excess emission at the Spitzer/MIPS wavelengths 24 and 70 μm, obtained from the four nominal runs. Since all disks have the same initial total mass (1 $M_\oplus$), the disks closer to the star are brighter and start to decay earlier. The difference between the excesses at 24 and 70 μm, a measure of the disks' effective temperature, is varying with radial distance as well. Thus, the convergence of just the 70 μm fluxes at later times is only coincidental.

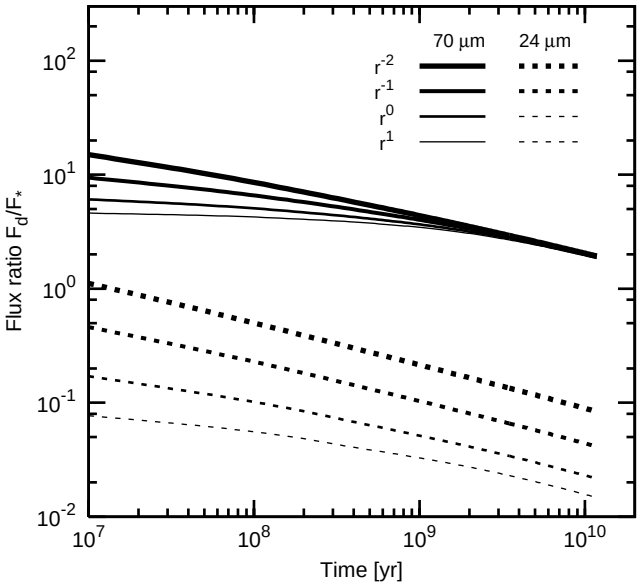


FIG. 13.— Time evolution of the infrared excess of extended disks with different initial radial distributions (labels indicate the radial slope of the surface mass density; the thicker lines, the flatter the profiles) at 24 μm (dashed lines) and 70 μm (solid lines). The total mass is $1M_\oplus$ in each case.

It is a result of the radial dependence of temperature and the collisional timescale.

5.3. *Fluxes from Extended Disks*

Since resolved debris disks suggest that the parent body reservoir in the disks is usually confined to a toroidal region (a planetesimal belt), or is made up of several such tori, it seems appropriate to simply combine individual rings without taking into account possible interactions between particles that belong to different rings. Thus, we summed up the fluxes from the four main runs. Different radial distributions in the whole disk were simulated by "weighting" the individual rings:

$$F_{\rm d} = \sum_{j=1}^{4} F_{\rm d,j}(r_j/r_0)^\gamma, \qquad (46)$$

where r_j are the central distances of the rings and values of 0, 1, 2, and 3 were used for the slope γ. As the reference runs were made for rings of one earth mass each with volumes proportional to r^3, the corresponding volume density in the extended disk is proportional to $r^{\gamma-3}$, while the pole-on surface density and normal geometrical optical depth follow $\propto r^{\gamma-2}$. The distance r_0 normalizes the total mass to $1M_\oplus$. Therefore, by changing the slope, the mass is only shifted between inner and outer regions.

In Fig. 13 the effect on the 24 and 70 μm fluxes is shown. If the weights are assigned in favor of more distant debris rings, the resulting fluxes are naturally reduced. The same is true for the speed of the decay because the timescales get longer. The evolution of the fluxes at the two Spitzer/MIPS wavelengths 24 and 70 μm differs significantly. At 24 μm the decay starts earlier and reaches its maximum speed earlier because shorter-lived inner regions make the main contribution.

The models contain a sufficient number of parameters, variation of which would affect the curves in Fig. 13 in different ways. As stated earlier, varying the total mass changes the timescale according to $\tau \propto M_{\rm disk}^{-1}$. Hence, the curves can be shifted along the lines of equal $t \cdot M_{\rm disk}$, i.e. along the top

left – bottom right diagonal. As seen from Fig. 13, variation of the radial distribution changes both the absolute level and the tilt of the curves. Besides, it affects the disk colors, i.e. the separation of the 24 and 70 μm curves in Fig. 13. In addition, the dynamical timescales, and therefore the tilt of the curves, are affected by eccentricities and inclinations of the parent bodies that may reflect the presence of planetary perturbers in the disk (see Sect. 3.3). Altogether, these degrees of freedom would allow one to reproduce a broad set of observational data.

6. COMPARISON WITH OBSERVATIONAL DATA

6.1. *Spitzer Data*

The advent of the Spitzer Space Observatory has brought a tremendous increase in the number of main-sequence stars surveyed for the existence of cold dust emission (see Werner et al. (2006) for a recent compilation).

The wealth of data from these debris disk surveys allows us to confront our models with actual observations. To this end, we searched the literature for published flux ratios at 24 and/or 70 μm (two of the three MIPS bands) around G-type main-sequence stars. To qualify as a main-sequence star we applied a lower limit to the stellar age of 10 Myr. Sources with stellar age estimates younger than this are likely stars with gas-dominated, protoplanetary disks; these were not taken into account.

The bulk of the data taken in the framework of the Legacy program "Formation and Evolution of Planetary Systems" (FEPS) (Meyer et al. 2004, 2006) is public since December 2006. The FEPS archive contains images, spectra, photometry tables and Kurucz photosphere models and is available at http://data.spitzer.caltech.edu/popular/feps/20061223_enhanced_v1/. Age estimates have been published for 46 FEPS G stars (Kim et al. 2005; Stauffer et al. 2005; Silverstone et al. 2006).

The large Guaranteed Time Observer (GTO) survey of FGK stars contains another 64 stars, where ages are available (Beichman et al. 2005, 2006a; Bryden et al. 2006). Data for ten more G stars are listed in Chen et al. (2005a,b). In total, 120 G-type main-sequence stars with flux ratios at 24 and/or 70 μm have been compiled from the literature for comparison with model flux ratios.

6.2. *Population Synthesis*

Based on the analytic prescription presented in Sect. 4 and motivated by the Wyatt et al. (2007b) work, we now build a synthetic set of debris disks around G2 stars. We generate a set of ring-like disks of width $\mathrm{d}r$ located at distances $r \in [r_{\min}, r_{\max}]$, with masses $M_{\rm disk} \in [M_{\min}, M_{\max}]$, and ages between 10 Myr and 10 Gyr. The probability to have a disk of initial mass M_0 at radius r was assumed to follow $M_0^{-1} r^{-0.8}$, where M_0^{-1} corresponds to a log-normal distribution of initial disk masses and the $r^{-0.8}$ dependence was proposed by Wyatt et al. (2007b). As described in Sect. 5.2, the temperatures and the resulting thermal fluxes are calculated using the modified black-body formulas by Backman & Paresce (1993), assuming the emitting grains to have $s = 1$ μm, in agreement with the size distribution shown in Fig. 4. The other parameters are taken to be: $q_{\rm p} = 2.00$, $q_{\rm g} = 1.67$, $q_{\rm s} = 1.877$, $\mathrm{d}r/r = 0.5$, $2I = e = 0.15$, $Q_{\rm D}^*(1\ {\rm m}) = Q_{\rm D}^*(1\ {\rm km}) = 5 \times 10^6$ erg/g, $b_{\rm d} = -0.12$, $b_{\rm g} = 0.47$, roughly corresponding to basalt in Benz & Asphaug (1999). Due to the small observational sample, our aim was not to perform a multi-parameter fit to the observations, but rather to cover the range of observed flux densities, which is defined by the limits of the distributions, not by their slopes.

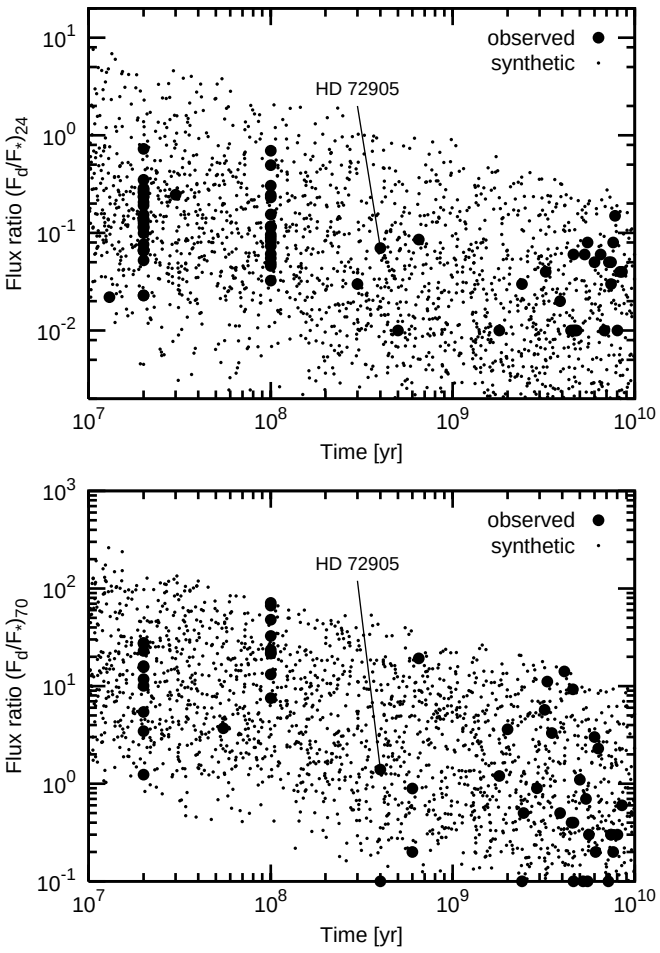


FIG. 14.— Flux ratios versus time for 24 μm *(top)* and 70 μm *(bottom)*. The synthesized population (*small dots*) is compared to the observed one (*big dots*). Individually labeled is the possibly transient system HD 72905, see text.

Varying disk locations and masses easily reproduces the observed distribution of fluxes at 24 μm and 70 μm (Fig. 14). The synthetic population shown corresponds to $r_{\min} \approx 20$ AU, $r_{\max} \approx 120$ AU and $M_{\min} < 0.01\ M_\oplus$, $M_{\max} \approx 30\ M_\oplus$. Here, the radial range is needed to cover the range of colors, i.e. the ratios between the excess emissions at the two wavelengths. The mass range is needed to cover the observed range of excess, especially for younger disks at 70 μm.

Analyses of Spitzer detections might indicate a statistically significant increase of both 24 and 70 μm fluxes at ages between a few tens of Myr to a few hundreds of Myr. (e.g., J. M. Carpenter et al., in prep.), which can only be marginally seen in our sample (Fig. 14). It is hypothesized that this feature is caused either by an increased dust production due to delayed stirring by growing planets or by events similar to the late heavy bombardment in the solar system. Such effect could only be studied with an improved version of our analytic model or with the numerical one.

The distribution of disk colors is more difficult to reproduce. Fig. 15 shows a significant abundance of fainter but warmer disks in an area that is not covered by the synthetic population. One explanation would be that the upper mass

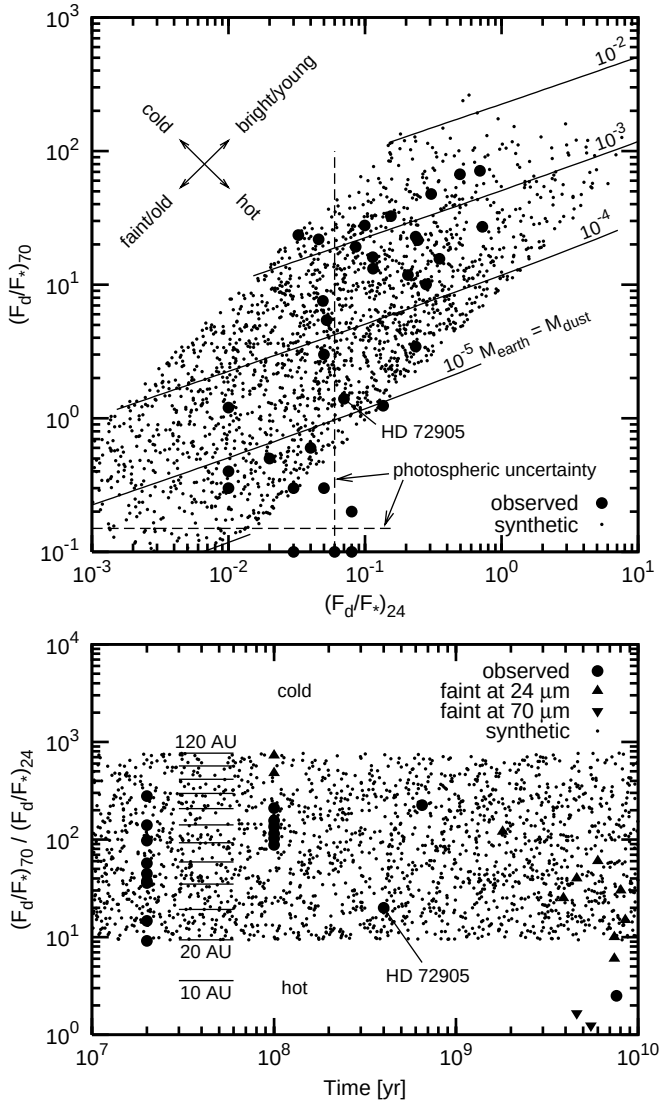


FIG. 15.— Relation between fluxes at 24 and 70 μm versus time. The synthesized population (*small dots*) is compared to the observed one (*big dots and triangles*). The average photospheric uncertainty for both filters is marked by dashed lines in the upper panel. Excesses below those limits in either of the two filters are marked by triangles in the lower panel. In addition, the upper panel shows lines of equal dust mass and the lower panel gives the ring radii corresponding to the colors.

limit is a function of radial distance, and that the innermost disks tend to be less massive and less luminous, from the very beginning. In addition, the lower panel of that Fig. 15 shows a trend towards higher effective temperatures for higher ages, which is difficult to understand. Indeed, as long as faint close-in disks are observed around older stars, one would expect ever brighter disks, and therefore more numerous detections of disks at the same distances around younger stars. Furthermore, the trend in question contradicts to the results by Najita & Williams (2005), who found no significant correlation between the disk radii and ages. Most likely, the discrepancy is only caused by uncertainties of the measured excesses at 24 μm. Bryden et al. (2006) report that the average photometric accuracy in that filter band is only as good as $1\sigma_{24} = 6\%$ due to stellar photosphere fitting errors and flat-field uncertainties. Therefore, excesses below those 6% of the photospheric emission cannot be considered as significant. For 70 μm, Bryden et al. (2006) state $1\sigma_{70} \approx 15\%$. Both limits are shown in the upper panel of Fig. 15.

In Figs. 14 and 15, there is one particular system directly labeled. That system, HD 72905, was observed to show significant excess emission not only at 24 and 70 μm, but also in the spectral ranges 8–13 and 30–34 μm of the Spitzer/IRS instrument (Beichman et al. 2006b). The presence of two dusty regions was suggested: one exozodiacal at 0.03–0.43 AU and one around 14 AU. From the excess at 8–13 μm, Wyatt et al. (2007a) inferred the dust population in HD 72905 to be transient because the observed fractional luminosity is above the maximum expected for a system of 300–400 Myr. As long as only 24 and 70 μm are considered, the HD 72905 dust does not seem particularly hot or bright, although it is among the hotter disks.

At this point, it is interesting to compare our results to those of Wyatt et al. (2007b). Both analytic approaches aim at explaining and reproducing the observations. Our model is different from theirs in that we take into account the size dependence of the critical specific energy as well as the transition from a "primordial" size distribution of planetesimals to the one set up by a collisional cascade. The amount of dust in their model is determined, from the very beginning, by the rather long collisional timescales of objects of tens of kilometers, so that the collisional evolution is much slower. This can be seen from the equations: "1+" in the denominator of Eq. (10) causes the mass to stay almost at the initial level for a long time, before the system reaches the t^{-1} decay. In our model, although the mass decay is asymptotically slower (t^{ξ} with $\xi \approx -0.3 \ldots -0.4$), it sets up very quickly, namely on collisional timescales of objects with minimum binding energy ($s_b \sim 100$ meters). Therefore, we would expect the model by Wyatt et al. (2007b) to show significantly larger excesses at ages considered, if all other parameters were comparable. This, however, is not the case. Wyatt et al. (2007b) assumed a much weaker material in their collisional prescription. Their $Q^*_{\rm D} = 300$ J/kg at an object radius of 30 km ($D_{\rm c} = 60$ km) is by more than two orders of magnitude below the values we use in Eq. (1). As $\tau \propto Q_{\rm D}^{q_{\rm P}-1}$ in Eq. (34), their collisional timescales are shorter and their evolution faster, too. Besides the material strength, the difference in the assumed effective eccentricities — $e = 0.05$ in their model against $e_{\max}/2 = 0.15$ in ours — causes another factor of roughly 10 in the collisional timescales, according to Sect. 3.3. All the differences listed happen to nearly compensate each other. As a net result, the excesses predicted by Wyatt's et al. and our models are comparable with each other (see also Fig. 11), being in reasonable agreement with the observed ones.

7. SUMMARY AND CONCLUSIONS

We investigated the long-term evolution of debris disks around solar-type (G2V) stars. Firstly, we performed numerical simulations with our collisional code. Secondly, the numerical results were supplemented by, and interpreted through, a new analytic model. The latter is similar to, and builds up on, the model developed earlier by Wyatt et al. (2007a), but extends it in several important directions. It naturally includes the transition from the "primordial" size distribution of left-over planetesimals, set up at their agglomeration phase, to the size distribution established by the collisional cascade. Further, it lifts the assumption that the critical specific energy needed for disruption is constant across the full range of sizes, from dust to the largest planetesimals. With these improvements, a good agreement between the numerics

and analytics is achieved.

We draw the following conclusions:

1. The timescale of the collisional evolution is inversely proportional to the initial disk mass. For example, halving the total mass doubles all collisional timescales. This rule is valid for systems where collisions are the only loss mechanism of particles and only as long as β-meteoroids are unimportant for the collisional budget.

2. Numerics and analytics consistently yield a $\tau \propto r^{4.3}$ dependence of the timescale of the collisional evolution on the radial distance.

3. Numerical simulations show that the collisional timescale varies with the average eccentricity of dust parent bodies as $\tau \propto e^{-2.3}$. The analytic approach suggests a somewhat weaker dependence, $\tau \propto e^{-5/3}$.

4. An evolving three-slope size distribution is proposed to approximate the numerical results. The biggest objects are still distributed primordially, with a slope $q_{\rm p}$. The objects below a certain transitional size are already reprocessed by collisions and thus have a quasi-steady-state size distribution, determined by their self-gravity (for intermediate-sized objects, slope $q_{\rm g}$) or by material strength (for smallest objects, slope $q_{\rm s}$). That transitional size corresponds to the largest objects for which the collisional lifetime is still shorter than the age of the system. The transitional size increases with time, meaning that ever-larger planetesimals get involved into the collisional cascade.

5. At actual ages of debris disks, $\sim$10 Myr to $\sim$10 Gyr, the decay of the dust mass and the total disk mass follow *different* laws. The reason is that, in all conceivable debris disks, the largest planetesimals have longer collisional lifetimes than the system's age, and therefore did not have enough time to reach collisional equilibrium. If the system were let to evolve for sufficiently long time, both dust mass and disk mass would start to follow t^{-1}. However, this requires time spans of much longer than 10 Gyr.

6. The loss rate of the dust mass, and the decay rate of fractional luminosity, primarily depend on the difference between the slope $q_{\rm p}$ of the "primordial" size distribution of largest planetesimals and the slope $q_{\rm g}$ of the size distribution of somewhat smaller, yet gravity-dominated, planetesimals that already underwent sufficient collisional evolution. With "standard" values of $q_{\rm p}$ and $q_{\rm g}$, the dust mass and the thermal fluxes follow approximately t^{ξ} with $\xi = -0.3 \ldots -0.4$.

7. Specific decay laws of the total disk mass and the dust mass largely depend on a few model parameters. Most important are: the critical fragmentation energy $Q^*_{\rm D}$ as a function of size, the slope of the "primordial" size distribution of planetesimals $q_{\rm p}$ and their maximum size $s_{\rm max}$, and the characteristic eccentricity e and inclination I of planetesimals.

8. The property that the maximum possible dust luminosity for a given age does not depend on the initial disk mass, established by Wyatt et al. (2007a), is only valid in cases of very rapid collisional evolution, i.e. in closer-in or dynamically very hot disks. For most of the systems at ages < 10 Gyr, an increase of the initial disk mass leads to an increase of the dust luminosity, unless that initial mass is assigned extreme values, incompatible with our understanding of planetesimal disks.

9. Assuming standard material prescriptions and disk masses and extents, a synthetic population of disks generated with our analytic model generally agrees with the observed statistics of 24 and 70 μm fluxes versus age. Similarly, the synthetic [24]-[70] colors are consistent with the observed disk colors.

As every model, our numerical model makes a number of general simplifying assumptions; the analytic one imposes further simplifications:

- The collisional evolution is assumed to be smooth and unperturbed. Singular episodes like the aftermath of giant break-ups or special periods of the dynamical evolution such as the late heavy bombardment are not included.

- Effects of possible perturbing planets are taken into account only indirectly: through the eccentricities of planetesimals (dynamical excitation) and confinement of planetesimal belts (truncation of disks). Further effects such as resonant trapping or ejection of material by planets are neglected.

- We only consider disruptive collisions. This is a reasonable approximation for disks that are sufficiently "hot" dynamically. However, cratering collisions become important when the relative velocities are insufficient for disruption to occur.

- Neither dilute disks under the regime of Poynting-Robertson drag nor very dense disks with collisional timescales shorter than orbital timescales and with avalanches (Grigorieva et al. 2007) are covered by the present work.

- Explaining the initial conditions or deriving them from the dynamical history of the systems at early stages of planetesimal and planetary accretion was out of the scope of this paper. Correlations between disk masses, disk radii, and the presence of planets, for example, were not considered, although they might alter the scalings we found here.

Despite these limitations, our models reproduce, in essential part, the observed evolution of dust in debris disks. We hope that they may serve as a starting point for in-depth studies that will certainly be undertaken in the future, motivated by questions that remain unanswered, as well as by new data expected from ongoing and planned observational programs.

We wish to thank Jean-François Lestrade, Philippe Thébault, and Mark Wyatt for fruitful discussions and Amaya Moro-Martín for useful review comments. This research has been partly funded by the Deutsche Forschungsgemeinschaft (DFG), project Kr 2164/5-1.

REFERENCES

Artymowicz, P. 1997, Ann. Rev. Earth Plan. Sci., 25, 175
Augereau, J. & Beust, H. 2006, A&A, 455, 987
Aumann, H. H., Beichman, C. A., Gillett, F. C., et al. 1984, ApJ, 278, L23
Backman, D. E. & Paresce, F. 1993, in Protostars and Planets III, ed. E. H. Levy & J. I. Lunine, 1253–1304
Beichman, C. A., Bryden, G., Rieke, G. H., et al. 2005, ApJ, 622, 1160
Beichman, C. A., Bryden, G., Stapelfeldt, K. R., et al. 2006a, ApJ, 652, 1674
Beichman, C. A., Tanner, A., Bryden, G., et al. 2006b, ApJ, 639, 1166
Benz, W. & Asphaug, E. 1999, Icarus, 142, 5
Bernstein, G. M., Trilling, D. E., Allen, R. L., et al. 2004, AJ, 128, 1364
Bryden, G., Beichman, C. A., Trilling, D. E., et al. 2006, ApJ, 636, 1098
Campo Bagatin, A., Cellino, A., Davis, D. R., Farinella, P., & Paolicchi, P. 1994, Planet. Space Sci., 42, 1079
Chen, C. H., Jura, M., Gordon, K. D., & Blaylock, M. 2005a, ApJ, 623, 493
Chen, C. H., Patten, B. M., Werner, M. W., et al. 2005b, ApJ, 634, 1372
Chen, C. H., Sargent, B. A., Bohac, C., et al. 2006, ApJS, 166, 351
Davis, D. R. & Ryan, E. V. 1990, Icarus, 83, 156
Dohnanyi, J. W. 1969, J. Geophys. Res., 74, 2531
Dominik, C. & Decin, G. 2003, ApJ, 598, 626
Durda, D. D. & Dermott, S. F. 1997, Icarus, 130, 140
Fujiwara, A. 1986, Memorie della Societa Astronomica Italiana, 57, 47
Fujiwara, A., Kamimoto, G., & Tsukamoto, A. 1977, Icarus, 31, 277
Gorlova, N., Rieke, G. H., Muzerolle, J., et al. 2006, ApJ, 649, 1028
Greaves, J. S. 2005, Science, 307, 68
Greaves, J. S. & Wyatt, M. C. 2003, MNRAS, 345, 1212
Grigorieva, A., Artymowicz, P., & Thébault, P. 2007, A&A, 461, 537
Jura, M., Chen, C. H., Furlan, E., et al. 2004, ApJS, 154, 453
Kenyon, S. J. & Bromley, B. C. 2004, AJ, 128, 1916
Kim, J. S., Hines, D. C., Backman, D. E., et al. 2005, ApJ, 632, 659
Krivov, A. V., Löhne, T., & Sremčević, M. 2006, A&A, 455, 509
Krivov, A. V., Mann, I., & Krivova, N. A. 2000, A&A, 362, 1127
Krivov, A. V., Sremčević, M., & Spahn, F. 2005, Icarus, 174, 105
Laor, A. & Draine, B. T. 1993, ApJ, 402, 441
Lestrade, J.-F., Wyatt, M. C., Bertoldi, F., Dent, W. R. F., & Menten, K. M. 2006, A&A, 460, 733
Liu, M. C., Matthews, B. C., Williams, J. P., & Kalas, P. G. 2004, ApJ, 608, 526
Matthews, B. C., Greaves, J. S., Holland, W. S., et al. 2007, PASP, 119, 84
Meyer, M. R., Hillenbrand, L. A., Backman, D., et al. 2006, PASP, 118, 1690
Meyer, M. R., Hillenbrand, L. A., Backman, D. E., et al. 2004, ApJS, 154, 422
Michel, P., Tanga, P., Benz, W., & Richardson, D. C. 2002, Icarus, 160, 10
Moór, A., Ábrahám, P., Derekas, A., et al. 2006, ApJ, 644, 525
Najita, J. & Williams, J. P. 2005, ApJ, 635, 625
O'Brien, D. P. & Greenberg, R. 2003, Icarus, 164, 334
Pan, M. & Sari, R. 2005, Icarus, 173, 342
Paolicchi, P., Verlicchi, A., & Cellino, A. 1996, Icarus, 121, 126
Rieke, G. H., Su, K. Y. L., Stansberry, J. A., et al. 2005, ApJ, 620, 1010
Silverstone, M. D., Meyer, M. R., Mamajek, E. E., et al. 2006, ApJ, 639, 1138
Spangler, C., Sargent, A. I., Silverstone, M. D., Becklin, E. E., & Zuckerman, B. 2001, ApJ, 555, 932
Stauffer, J. R., Rebull, L. M., Carpenter, J., et al. 2005, AJ, 130, 1834
Strubbe, L. E. & Chiang, E. I. 2006, ApJ, 648, 652
Su, K. Y. L., Rieke, G. H., Stansberry, J. A., et al. 2006, ApJ, 653, 675
Tanga, P., Cellino, A., Michel, P., et al. 1999, Icarus, 141, 65
Tedesco, E. F., Cellino, A., & Zappalá, V. 2005, AJ, 129, 2869
Thébault, P. & Augereau, J.-C. 2007, A&A, 472, 169
Thébault, P., Augereau, J. C., & Beust, H. 2003, A&A, 408, 775
Trujillo, C. A., Jewitt, D. C., & Luu, J. X. 2001, AJ, 122, 457
Werner, M., Fazio, G., Rieke, G., Roellig, T. L., & Watson, D. M. 2006, ARA&A, 44, 269
Wyatt, M. C. 2005, A&A, 433, 1007
Wyatt, M. C., Smith, R., Greaves, J. S., et al. 2007a, ApJ, 658, 569
Wyatt, M. C., Smith, R., Su, K. Y. L., et al. 2007b, ApJ, 663, 365